https://doi.org/10.5194/egusphere-2025-3556
Preprint. Discussion started: 8 October 2025

Data-driven equation discovery of a sea ice albedo parametrisation

Diajeng W. Atmojo[1,2], Katja Weigel[1,2], Arthur Grundner[2], Marika M. Holland[3], Dmitry Sidorenko[4], and Veronika Eyring[2,1]

[1]University of Bremen, Institute of Environmental Physics (IUP), Bremen, Germany
[2]Deutsches Zentrum für Luft- und Raumfahrt e.V. (DLR), Institut für Physik der Atmosphäre, Oberpfaffenhofen, Germany
[3]National Center for Atmospheric Research, Boulder CO, USA
[4]Alfred Wegener Institute, Helmholtz Centre for Polar and Marine Research (AWI), Bremerhaven, Germany

Correspondence: Diajeng W. Atmojo (atmojo@uni-bremen.de)

Abstract. In the Finite-Element Sea Ice Model (FESIM), a part of the Finite-Element Sea ice Ocean Model (FESOM), sea ice albedo is treated as a tuning parameter defined by four constant values depending on snow cover and surface temperature. This parametrisation is too simple to capture the spatiotemporal variability of observed sea ice albedo. Here, we aim for an improved parametrisation by discovering an interpretable, physically consistent equation for sea ice albedo using symbolic regression, an interpretable machine learning technique, combined with physical constraints. Leveraging daily pan-Arctic satellite and reanalyses data from 2013 to 2020, we apply sequential feature selection which identifies snow depth, surface temperature, sea ice thickness and 2 m air temperature as the most informative features for sea ice albedo. As a function of these features, our data-driven equation identifies two critical mechanisms for determining sea ice albedo: the high sensitivity of sea ice albedo to small changes in thin snow and a weighted difference of the sea ice surface and 2 m air temperature, serving as a seasonal proxy that indicates the transition between melting and freezing conditions. To understand how additional model complexity reduces errors, we evaluate our discovered equation against baseline models with different complexities, such as multilayer perceptron neural networks (NNs) and polynomials on an error-complexity plane, showing that the equation excels in balancing error and complexity and reduces the mean squared error by about 51% compared to the current FESIM parametrisation. Unlike NNs, our discovered equation allows for further regional and seasonal analyses due to its inherent interpretability. By fine-tuning its coefficients we uncover differences in physical conditions that drive sea ice albedo. This study demonstrates that learning an equation from observational data can deepen the process-level understanding of the Arctic Ocean's surface radiative budget and improve climate projections.

1 Introduction

Sea ice, formed from frozen sea water, modulates the transfer of heat, moisture, and momentum between the ocean and the atmosphere (Stroeve and Notz, 2018). During spring and summer, its high albedo allows it to reflect a large amount of incoming solar radiation, whereas during winter, it insulates the colder atmosphere from the relatively warm ocean (Hunke et al., 2010). In recent decades, observations have shown a decrease in the extent and thickness of Arctic sea ice (Kwok, 2018). Most Coupled Model Intercomparison Project Phase 6 (CMIP6) models (Eyring et al., 2016) project the disappearance of multiyear ice, i.e.

https://doi.org/10.5194/egusphere-2025-3556
Preprint. Discussion started: 8 October 2025

ice that remains for at least one summer, before 2050 in all CO_2 emission scenarios (Notz and Community, 2020). Thinner and younger sea ice, prevalent due to these changes, has a lower albedo, which leads to a higher absorption of the solar radiation by the sea ice surface, thereby promoting sea ice melting and the formation of melt ponds (Perovich et al., 2002; Light et al., 2022; Niehaus et al., 2024). The loss of sea ice exposes the darker ocean, increasing solar absorption and accelerates the melting of remaining ice (Curry et al., 1995; Stroeve and Notz, 2018). This cycle, termed the ice-albedo feedback, is the second leading feedback mechanism for Arctic amplification, following the lapse-rate feedback (Pithan and Mauritsen, 2014).

However, a wide spread remains in the projections of Arctic sea ice extent and volume across all CMIP6 models and little improvement in overall model performance has been achieved along the previous CMIP phases (Selivanova et al., 2024). One of the main sources of uncertainty in projecting Arctic sea ice is the representation of sea ice albedo (α), which has been oversimplified in ESMs (Curry et al., 2001; Pirazzini, 2009). Over the past decades, sea ice albedo parametrisations of various complexities have been developed by incorporating spectral band dependencies (Holland et al., 2012), cloud conditions (Jäkel et al., 2024), and explicitly resolving melt ponds (Flocco et al., 2010; Hunke et al., 2013). More sophisticated models use sea ice radiative transfer schemes that compute an albedo from inherent optical properties, including those of ice, snow, ponds, and included absorbers (black carbon, algae) instead of prescribing an albedo based on surface type (Briegleb and Light, 2007; Holland et al., 2012).

The Finite-Element Sea Ice Model (FESIM; Danilov et al., 2015), part of the Finite-Element Sea ice Ocean Model (FESOM; Danilov et al., 2017), employs a very simplified sea ice albedo parametrisation based on Parkinson and Washington (1979, hereafter PW79). In FESIM, PW79 is augmented with an implicit treatment of melt ponds by distinguishing between melting and non-melting conditions. Fixed broadband albedo values are assigned to four surface types: snow-covered ice ($\alpha = 0.81$), bare ice ($\alpha = 0.7$), wet (melting) snow ($\alpha = 0.77$), and wet (melting) ice ($\alpha = 0.68$). Following a zero-layer thermodynamic scheme (Parkinson and Washington, 1979), FESIM uses these four values as tuning parameters to compensate for other biases within the model. Thus, the spatiotemporal variability of sea ice albedo is not captured in its full complexity. We argue that a more realistic formulation of the sea ice albedo is needed to disentangle model errors resulting from the thermodynamic scheme.

Machine learning (ML) has become a pivotal tool in Earth system science. The era of big data originating from a diversity of observational products, reanalyses and climate data from CMIP models provides high-dimensional datasets that ML can leverage to reveal hidden patterns and accelerate discoveries beyond conventional approaches (Eyring et al., 2024; Vance et al., 2024; Bracco et al., 2024; Camps-Valls et al., 2023). In particular, data-driven equation discovery, an interpretable ML method, has the potential to bridge the gap between the ML and Earth system science community by providing transparency and reliability in ML predictions. Analytical expressions identified from data allow the user to interpret the ML prediction ad hoc, providing trustworthiness in the decision-making process of the ML algorithm and advancing scientific discoveries (Huntingford et al., 2025; Song et al., 2024). Use cases in Earth system modelling focus on improving the representation of subgrid processes, such as the representation of clouds (Grundner et al., 2024) and ocean eddies (Zanna and Bolton, 2020). Integrating ML with physical modelling aims to create hybrid Earth system models (ESMs) that combine traditional physics-

https://doi.org/10.5194/egusphere-2025-3556
Preprint. Discussion started: 8 October 2025

based frameworks with data-driven methods, offering a promising pathway to improve climate projections and deepen our understanding of the Earth system (Rasp et al., 2018; Camps-Valls et al., 2023; Eyring et al., 2024).

This study applies symbolic regression, a data-driven equation discovery approach, to discover an equation for sea ice albedo directly from observational data, improving upon the simple PW79 sea ice albedo parametrisation within FESIM. Our aim is to derive a simple and physically consistent equation using the PySR library (Cranmer et al., 2020), leveraging satellite and reanalyses data. Following Beucler et al. (2024) and Grundner et al. (2024), we adopt a Pareto-optimal strategy, identifying parsimonious models that perform well using few input features. This approach reduces model complexity while maintaining accuracy and improves comprehensibility and interpretability. We address the following main questions:

1. Do we find a physically consistent equation for sea ice albedo using data-driven equation discovery that performs better than PW79 based on reanalysis data and observations?

2. Do we improve our physical understanding of the surface radiative budget of the Arctic Ocean with our data-driven equation and discover deficiencies in how sea ice thermodynamics are treated in FESIM?

This paper is organised as follows: Section 2 outlines the satellite and reanalysis data and the methodologies used in the Pareto-optimality framework, including data preprocessing, multilayer perceptron neural network (NN) hyperparameter tuning, sequential feature selection (SFS), and model complexity and error evaluation. Section 3 provides a physical interpretation of the best-performing equation, while Sec. 4 compares this equation with PW79 and baseline models, including the trained NN and polynomials, on our observational dataset. Section 5 demonstrates the versatility of the equation through regional and monthly optimisations, and Sec. 6 offers conclusions and future perspectives.

2 Material and methods

2.1 Data

This study integrates multiple data products from satellites and reanalyses listed in Table 1, which we carefully select to ensure high-quality coverage of the entire pan-Arctic region on a daily basis. Furthermore, we only consider variables available both in FESIM and FESOM since these are our target ocean-sea ice models. By intersecting the temporal and spatial domains of the data products, the overlapping period is from 2013 to 2020, during the months of March to September when sunlight is present in the whole pan-Arctic region. The final dataset consists of five sea ice and five atmospheric input features. For better readability, we refer to input features as features.

2.1.1 Satellite data

The Polar Pathfinder - Extended Climate Data Record (CDR) product (Key et al., 2016, 2001) includes broadband albedo, surface temperature ($T_{0\mathrm{m}}$), and binary cloud mask (clear-sky/cloudy) with a temporal resolution of 12 hours and a spatial

https://doi.org/10.5194/egusphere-2025-3556
Preprint. Discussion started: 8 October 2025

Table 1. Description of variables used in this study. Reanalysis data products are italised. The final dataset covers the years 2013–2020 as this is the period where the temporal coverages of all data products coincide.

Variable	Source	Spatial resolution	Temporal resolution
Output			
Surface broadband albedo	VIIRS	25 km	12 hourly
Features - Sea ice variables			
Sea ice thickness (h_{ice})	CS2SMOS	25 km	daily
	TOPAZ4	12.5 km	daily
Snow depth (h_{snow})	AMSR2	25 km	daily
	TOPAZ4	12.5 km	daily
Sea ice speed	NSIDC	25 km	daily
Surface temperature (T_{0m})	VIIRS	25 km	12 hourly
Age of sea ice	NSIDC	12.5 km	weekly
Features - Atmospheric variables			
2 m temperature (T_{2m})	*ERA5*	0.25°	hourly
Rain (cumsum of last 7 days)	*ERA5*	0.25°	hourly
Snowfall (cumsum of last 7 days)	*ERA5*	0.25°	hourly
Relative humidity (RH)	*ERA5*	0.25°	hourly
10 m wind speed	*ERA5*	0.25°	hourly
For masking purposes (see Sec. 2.2.1)			
Sea ice concentration	CS2SMOS	25 km	daily
	TOPAZ4	12.5 km	daily
	AMSR2	3.125 km	daily
Cloud cover	VIIRS	25 km	12 hourly
Surface downward thermal radiation, all-sky	*ERA5*	0.25°	hourly
Surface downward thermal radiation, clear-sky	*ERA5*	0.25°	hourly

resolution of 25 km. From 2013 until 2020, measurements are taken from the Visible Infrared Imaging Radiometer Suite (VIIRS). Compared with the SHEBA data, the albedo shows an uncertainty of about 7% (Key et al., 2001).

The Level 4 SMOS-CryoSat (CS2SMOS) merged product (Ricker et al., 2017) includes daily sea ice thickness (h_{ice}) and sea ice concentration on a 25 km grid for March and April. The uncertainty, ranging from 0.1 m to 0.5 m, is due to measurement inaccuracies and merging algorithms compared to airborne electromagnetic measurements.

https://doi.org/10.5194/egusphere-2025-3556
Preprint. Discussion started: 8 October 2025

The Advanced Microwave Scanning Radiometer 2 (AMSR2) satellite instrument provides daily snow depth data (h_{snow}) for March and April (Rostosky et al., 2018) and sea ice concentration data for the whole year (Spreen et al., 2008). Snow depth has a spatial resolution of 25 km, whereas sea ice concentration has a finer spatial resolution of 3.125 km. The uncertainty of snow depth is larger with increasing thickness, and slightly higher over multiyear ice than first year ice. Moreover, wrongly retrieved negative snow depth can occur over thin ice due to the signal coming from the ocean water. For sea ice concentrations below 65%, the uncertainty in measurements reaches a maximum of 25%, whereas at higher sea ice concentrations, the uncertainty is reduced to less than 10%. These uncertainties stem from instrument-related errors, variability in atmospheric and surface conditions, and sensitivity of the algorithm to independent measurement validation.

The Polar Pathfinder Daily 25 km EASE-Grid Sea Ice Motion Vectors (Version 4) product (Tschudi et al., 2019a), which integrates data from various observations and reanalyses, gives sea ice velocity information. The EASE-Grid Sea Ice Age (Version 4) product (Tschudi et al., 2019b), with a spatial resolution of 12.5 km, provides weekly sea ice age with a temporal resolution of a year, meaning that an age of one indicates that the sea ice is up to one year old.

2.1.2 Reanalyses data

Satellite-based data for sea ice and snow depth are confined to the winter months (October/November–March/April) due to the limitations of satellite retrieval methods arising from the presence of melt ponds in summer (Ricker et al., 2017; Rostosky et al., 2018). To fill the gaps in the summer months (May–September), we use daily data of snow depth, sea ice thickness, and sea ice concentration from the Arctic Ocean Physics Reanalysis *TOPAZ4b* (European Union-Copernicus Marine Service, 2020). We deem it reasonable to use reanalysis data to fill the gaps as the correlation matrices of the satellite and reanalysis data are comparable for March and April (see Appendix A1). *TOPAZ4b* operates at a 12.5 km spatial resolution available from 1991 to 2023, based on the HYCOM ocean model (Bleck, 2002) coupled to a zero-layer scheme (Parkinson and Washington, 1979) with the elastic-viscous-plastic (EVP) rheology (Hunke and Dukowicz, 1997). *ERA5* reanalysis data is used as forcing at the ocean surface. Sea ice concentration is assimilated with OSI-SAF (European Union-Copernicus Marine Service, 2015), while sea ice thickness data is assimilated with CS2SMOS. Observations reveal that sea ice concentration on the sea ice edges retreats too rapidly in early summer and refreezes too fast in early winter, with the thicker sea ice being underestimated. Snow depth is also underestimated, noticeably in June. From the *ERA5* reanalysis product (Copernicus Climate Change Service, 2018a, b), we acquire hourly atmospheric surface data on a regular 0.25° longitude/latitude grid: 2 m temperature ($T_{2\text{m}}$), rain, snowfall, relative humidity (RH), and 10 m wind speed, and surface downward thermal radiation under all-sky and clear-sky conditions.

2.2 Methods

Building on the principles outlined by Beucler et al. (2024) and Grundner et al. (2024), this study employs a Pareto optimality-based workflow as illustrated in Fig. 1.

https://doi.org/10.5194/egusphere-2025-3556
Preprint. Discussion started: 8 October 2025

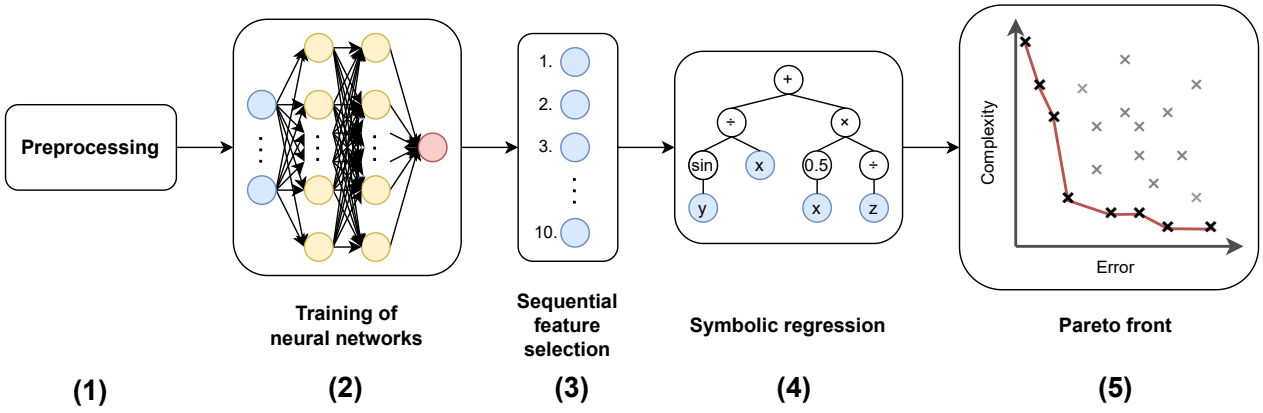

Figure 1. Pareto optimality-based workflow based on Beucler et al. (2024) and Grundner et al. (2024), exemplarily for discovering equations with symbolic regression. The process involves: (1) preprocessing of observational and reanalyses data to ensure consistency for the machine learning workflow, (2) training of multilayer perceptron neural networks (NNs), (3) sequential feature selection (SFS) for dimensionality reduction and identification of key features out of ten features governing sea ice albedo, (4) symbolic regression as data-driven equation discovery approach, and (5) comparison between the best-performing equations and baseline models (polynomials and NNs with reduced feature sets chosen by the SFS algorithm) on an error-complexity plane to evaluate how increasing model complexity reduces error.

2.2.1 Data preparation

This section describes the efforts taken to reconcile the different datasets from Sec. 2.1 and to illustrate the combined regional and temporal coverage. Using xESMF (Zhuang et al., 2024), remapping all data products (Table 1) to a common daily frequency on the albedo grid as reference grid ensures consistency and reliability of the final dataset and little modification of the albedo values as albedo is our target variable.

For albedo, we rely exclusively on daytime data due to its higher accuracy compared to nighttime data. To increase the sampling frequency of the weekly sea ice age data, we address gaps by applying the age value of the week's first day across the subsequent days. For *ERA5* data, we calculate daily means for $T_{2\mathrm{m}}$, RH, 10 m wind speed, and surface downward thermal radiation under clear-sky and all-sky atmospheric conditions. Additionally, we adjust rain and snowfall data using a cumulative sum from the preceding seven days to consider a weekly memory effect. When transitioning from finer to a coarser grid, which is the case for *TOPAZ4*, NSIDC, *ERA5* data, and AMSR2 for sea ice concentration, we employ a conservative regridder that maintains the integral of the source field by computing a weighted area mean over intersecting grids. For h_{ice}, h_{snow}, sea ice speed and concentration from CS2SMOS, bilinear regridding is sufficient for smoothly varying variables which match the resolution of the target grid.

Furthermore, we perform two masking operations to ensure equivalent atmospheric conditions and consistent spatial coverage across both observational and reanalyses products: cloud and sea ice pack masking. In terms of cloud masking, we use data samples where cloud conditions match across all data products, discarding the transition zone between clear-sky and cloudy

https://doi.org/10.5194/egusphere-2025-3556
Preprint. Discussion started: 8 October 2025

conditions as cloud cover in the VIIRS product is a binary variable, only distinguishing between clear-sky and cloudy conditions. Since the total cloud cover variable in *ERA5* is known to be overestimated in the Arctic region, Zampieri et al. (2023) proposed to compute the difference in surface downward thermal radiation between clear-sky and all-sky atmospheric conditions Δ_{STRD} to determine cloud conditions. Zampieri et al. (2023) defined $\Delta_{STRD} \leq 15\,\mathrm{W\,m^{-2}}$ to be clear-sky, $15\,\mathrm{W\,m^{-2}} < \Delta_{STRD} \leq 40\,\mathrm{W\,m^{-2}}$ as the transition zone and $\Delta_{STRD} > 40\,\mathrm{W\,m^{-2}}$ as cloudy. In addition, we only consider data samples where the sea ice concentration exceeds 80%, defining a sea ice pack, with the aim to isolate the effects of the sea ice surface without the influence of ocean water. To omit adjacency effects such as land contamination, we perform a land mask with a buffer of 50 km. Figure 2 shows the number of data samples per month and Arctic subregion defined by Meier and Stewart (2023). In total, the final dataset consists of 7,903,463 data samples, with the Central Arctic being the most dominant region with 5,060,064 data samples.

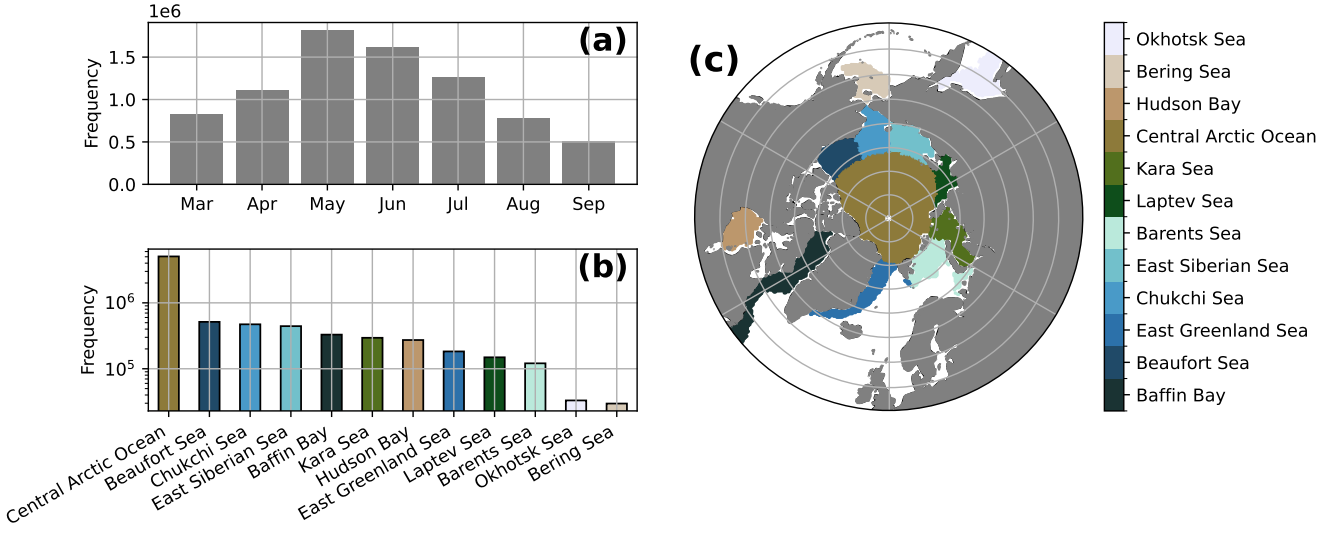

Figure 2. Panel (a) shows the monthly (March–September) and panel (b) the regional distribution of preprocessed dataset on a logarithmic y-axis with panel (c) illustrating the Arcitic subregions defined by Meier and Stewart (2023).

Let $\mathbf{X}$ be an $m \times n$ matrix representing the dataset, where m is the number of features, n is the number of samples and $\boldsymbol{\sigma} = (\sigma_1, \sigma_2, ..., \sigma_m) \in \mathbb{R}^m$ is the vector of standard deviations for each feature. For our machine learning workflow, we split the dataset temporally into a training (2013–2018) and validation set (2019–2020) and standardise each sample $\mathbf{X}_j \in \mathbb{R}^m$ by dividing the feature values $x_{i,j}$ by the corresponding standard deviation σ_i of the training set, yielding

$$\mathbf{Z}_j = \frac{\mathbf{X}_j}{\boldsymbol{\sigma}} = \left(\frac{x_{1,j}}{\sigma_1}, \frac{x_{2,j}}{\sigma_2}, ..., \frac{x_{m,j}}{\sigma_m} \right). \tag{1}$$

$\mathbf{Z}$ is the resulting $m \times n$ standardised dataset matrix, with standardised samples $\mathbf{Z}_j \in \mathbb{R}^m$. By this, we avoid preferential treatment of features that natively assume larger values.

https://doi.org/10.5194/egusphere-2025-3556
Preprint. Discussion started: 8 October 2025

2.2.2 Neural network architecture

We train a multilayer perceptron NN using PyTorch (Paszke et al., 2019) by setting the hyperparameters to the default values in PyTorch and refining the number of layers, hidden units, learning rate, and batch size manually (Table 2). We fix Adam as the optimiser and the mean squared error (MSE) as the loss function, which measures the mean squared difference between the model prediction $\alpha(\mathbf{Z}_j) \in \mathbb{R}$ (sea ice albedo) and the respective ground truth value y_j

$$\text{MSE} \overset{\text{def}}{=} \frac{1}{n}\sum_{j=1}^{n}(\alpha(\mathbf{Z}_j) - y_j)^2. \tag{2}$$

Table 2. Hyperparameters of multilayer perceptron neural network using PyTorch (Paszke et al., 2019).

Hyperparameters	Values
Number of layers	3
Number of units	32
Learning rate	0.001
Batch size	32
Optimiser	Adam

2.2.3 Sequential feature selection

Using the same NN architecture as described in Sec. 2.2.2, we use it as an estimator to perform forward SFS with *SequentialFeatureSelector* from the scikit-learn library (Pedregosa et al., 2011). SFS provides a ranking of feature importance which, in addition to helping us to maximise predictive performance using sparse models, can provide an intuition of the underlying physics. There are two reasons why we strive for reducing dimensionality: Symbolic regression performs best on low-dimensional data (see Sec. 2.2.4), and we seek parsimonious models, i.e. models that depend on few features to lower the model complexity and improve interpretability. Forward SFS begins by training the optimised NN with one feature and evaluating its performance based on the MSE on the validation set. The feature leading to the lowest MSE on the validation set can be considered to be the most informative from the set of features considered. In the following iterations, additional features are incorporated sequentially, retaining those that minimise the MSE. To reduce computational resources while still preserving robust results, we create ten subsets from the whole dataset with 10^5 data samples each and perform SFS on each subset. To retrieve the overall ranking of the features, we average the ranking of each feature across all subsets.

2.2.4 Symbolic regression

Symbolic regression fits equations to the dataset, searching through the space of mathematical expressions based on predefined mathematical operators $(+, -, \sin, ...)$. Following Grundner et al. (2024), we use the PySR library by Cranmer et al. (2020) due to its flexibility and high success rate in benchmarking tests (De Franca et al., 2024). PySR is based on genetic programming and implements tree-based candidate solutions with tournament selection, local leaf search, and multiple populations.

https://doi.org/10.5194/egusphere-2025-3556
Preprint. Discussion started: 8 October 2025

We find five features to be the practical upper bound which we retrieve from the ranking of our previous SFS results. Given that PySR is capable of discovering compact and interpretable equations of low complexity, it can operate effectively with a reduced dataset. Consequently, we downsample the training set to 10,000 data samples, leveraging the efficiency of PySR in handling limited data. Multiple runs of PySR with varying hyperparameters are needed as there is no guarantee that the discovered equations are optimal for their complexity, producing about 800 equations in total. We directly filter out equations with a storage size greater than 1500 bits to neglect long and complex equations.

To ensure physical consistency, the equations should satisfy the following physical constraints (PC): (1) The value of sea ice albedo α should be between 0 and 1; (2) snow depth h_{snow} significantly increases sea ice albedo (Grenfell and Maykut, 1977; Grenfell and Perovich, 2004); (3) under freezing conditions, thicker ice h_{ice} has a higher sea ice albedo than thinner ice (Perovich, 1996); (4) with rising surface temperature, sea ice melts, driving melt pond formation, which decreases the sea ice albedo significantly (Grenfell and Maykut, 1977; Perovich, 1996); (5) the function should be smooth over the entire domain. We can mathematically formalise these physical constraints for all samples $\mathbf{Z}_j$

$$\text{PC1}: \alpha(\mathbf{X}_j) \in [0,1]$$

$$\text{PC2}: \partial\alpha(\mathbf{X}_j)/\partial h_{\text{snow}} \geq 0$$

$$\text{PC3}: \partial\alpha(\mathbf{X}_j)/\partial h_{\text{ice}} \geq 0$$

$$\text{PC4}: \partial\alpha(\mathbf{X}_j)/\partial T_{0\text{m}} \leq 0$$

$$\text{PC5}: \alpha(\mathbf{X}_j) \text{ is a smooth function.}$$

As some equations are too complex to be solved analytically, each equation $\alpha(\mathbf{X})$ is checked for these PCs by approximating the first-order partial derivative with respect to a feature x with the central difference method

$$\frac{\partial\alpha}{\partial x} \approx \frac{\alpha(x+h) - \alpha(x-h)}{2h}, \tag{3}$$

where $h = 10^{-5}$ defines the step size for finite difference.

Keeping the physically consistent equations that satisfy all PCs, we perform a secondary optimisation on a subset of 10^5 data samples from the training set. This involves introducing an additional coefficient for each feature in the equation, unless PySR has already generated it. The *minimize* function from the SciPy library (Virtanen et al., 2020) allows a robust framework for minimisation using the Nelder-Mead (Nelder and Mead, 1965) and Broyden–Fletcher–Goldfarb–Shanno (BFGS) methods (Nocedal and Wright, 2006), common choices for general nonlinear optimisation problems.

2.2.5 Pareto-optimal models

Having found the best-performing equations that satisfy the PCs, we compare the equations with baseline models within an error-complexity graph, illustrating the gain of increasing model complexity with respect to the error. The baseline models are polynomials of degree one to four using *PolynomialFeatures* from the Scikit-learn library (Pedregosa et al., 2011), and the trained NN from Sec. 2.2.2. Furthermore, we also include the parsimonious NN models from Sec. 2.2.3. Likewise, we perform

https://doi.org/10.5194/egusphere-2025-3556
Preprint. Discussion started: 8 October 2025

SFS on the polynomials, analogous to how it is described in Sec. 2.2.3, and include them in the error-complexity graph. The measure of error is the MSE, while the model complexity is defined as the number of tunable parameters. Therefore, the model complexity can be increased in two ways: increasing the feature dimensionality and increasing the degree of a polynomial. For the NN architecture used in this study, adding one feature does not substantially increase the model complexity since adding one feature is equivalent to adding a single node in the NN.

3 Analysis of the best-performing equation

3.1 Feature importance in the baseline models

The numbers in brackets indicate the averaged ranking across the ten subsets. When no bracket is indicated, the ranking of a feature remains consistent across all subsets. Let $\mathcal{P}_d$ be a polynomial of degree $d \in \{1,2,3,4\}$. The SFS algorithm reveals the following feature rankings for $\mathcal{P}_{1-4}$ and NN:

$\mathcal{P}_1$: $h_{\text{snow}} \rightarrow T_{0\text{m}} \rightarrow T_{2\text{m}} \rightarrow$ rain $\rightarrow$ snowfall $\rightarrow h_{\text{ice}} \rightarrow$ RH $\rightarrow$ wind speed $\rightarrow$ ice speed $\rightarrow$ age

$\mathcal{P}_2$: $h_{\text{snow}} \rightarrow T_{0\text{m}} \rightarrow h_{\text{ice}} \rightarrow T_{2\text{m}} \rightarrow$ snowfall $\rightarrow$ RH $\rightarrow$ ice speed $(7.5) \rightarrow$ rain $(7.9) \rightarrow$ wind speed $(8.6) \rightarrow$ age

$\mathcal{P}_3$: $h_{\text{snow}} \rightarrow T_{0\text{m}} \rightarrow T_{2\text{m}} \rightarrow h_{\text{ice}} \rightarrow$ snowfall $\rightarrow$ RH $\rightarrow$ age $(7.1) \rightarrow$ wind speed $(8.8) \rightarrow$ rain $(8.9) \rightarrow$ ice speed (9.2)

$\mathcal{P}_4$: $h_{\text{snow}} \rightarrow T_{0\text{m}} \rightarrow h_{\text{ice}}\,(3.2) \rightarrow T_{2\text{m}}\,(3.9) \rightarrow$ RH $(6.6) \rightarrow$ age $(6.8) \rightarrow$ wind speed $(7.4) \rightarrow$ snowfall (7.6)
$\rightarrow$ ice speed $(8.2) \rightarrow$ rain (8.4)

NN : $h_{\text{snow}} \rightarrow T_{0\text{m}} \rightarrow h_{\text{ice}}\,(3.2) \rightarrow T_{2\text{m}}\,(3.8) \rightarrow$ snowfall $(5.6) \rightarrow$ RH $(7.0) \rightarrow$ rain $(7.8) \rightarrow$ wind speed (8.0)
$\rightarrow$ ice speed $(8.2) \rightarrow$ age (8.4)

In all model families, there is a consistent pattern in the ranking of the most informative features. All model types identify h_{snow} as the most informative predictor and $T_{0\text{m}}$ as the second most informative predictor. h_{snow} being the most informative predictor is plausible since snow is the most reflective medium in nature and, when present, constitutes the uppermost layer where solar radiation initially impacts. Snow has a low optical depth due to the scattering of incoming solar radiation in diffusive directions, implying that a snow layer of a few centimeters significantly increases surface albedo (Grenfell and Maykut, 1977). Additionally, at the spatial scales of our dataset (25 km), snow depth is likely related to snow fractional coverage which is also impactful for the albedo. $T_{0\text{m}}$ as the second most informative predictor is in agreement with the fact that $T_{0\text{m}}$ is a proxy of whether the surface is under melting or freezing conditions, as the presence of melting water reduces albedo. For instance, fresh snow exhibits a higher albedo compared to wet snow (Grenfell and Maykut, 1977). Sea ice albedo parametrisations that do not explicitly resolve melt ponds include the radiative effect of melt ponds implicitly with $T_{0\text{m}}$ (e.g. PW79). Excluding the linear model, the top predictors after h_{snow} and $T_{0\text{m}}$ are h_{ice} and $T_{2\text{m}}$. As sea ice has a higher optical depth than snow, h_{ice} ranked below h_{snow} seems plausible, implying that variations in h_{snow} may be more crucial to albedo than variations in h_{ice}.

The inclusion of $T_{2\text{m}}$ among the most informative predictors is unexpected given the high correlation (0.92) between $T_{0\text{m}}$ and $T_{2\text{m}}$ (see Appendix A2), which would suggest redundancy in $T_{2\text{m}}$, ranked below $T_{0\text{m}}$. Nevertheless, SFS quickly chooses

https://doi.org/10.5194/egusphere-2025-3556
Preprint. Discussion started: 8 October 2025

T_{2m} as an additional predictor after T_{0m} is accounted for, indicating that sea ice albedo is not only dependent on surface conditions, but is also influenced by atmospheric conditions near the surface, affecting the optical properties of the sea ice surface. Additionally, this may be in part due to the fact that T_{2m} can go above the melting point, whereas T_{0m} cannot. To the best of our knowledge, existing sea ice albedo parametrisations in ESMs with an implicit scheme of melt pond representation do not include T_{2m}. Sea ice models that explicitly resolve melt ponds, e.g. Flocco et al. (2010) and Hunke et al. (2013), use T_{2m} to compute the surface melting rate to calculate the melt water accumulation in the ponds.

In implicit schemes, the transition of T_{0m} around the freezing point of sea ice is used as information to implicitly determine melting and freezing conditions, which characterise the wetness of sea ice surface, altering sea ice optical properties. Examining in-situ measurements of T_{2m} from the MOSAiC expedition and satellite swath data of melt pond fraction with a resolution of 1.2 km, Niehaus et al. (2024) have reported that T_{2m} is one of the main driver of the formation and evolution of melt ponds, explaining short-lived changes in melt pond fractions and thus, decreasing albedo. Although they concluded that *ERA5* reanalysis data are not well suited to study local melt pond characteristics due to the coarse spatial resolution, here we show that T_{2m} of *ERA5* is a valuable predictor to understand the large-scale mechanisms that modulate sea ice albedo in the pan-Arctic region.

The ranking of the remaining features shows some variability across model families, but some patterns can be identified. For instance, snowfall and RH tend to be ranked higher than wind speed, ice speed, and age in most model families. On a large scale, features related to thermodynamics are more relevant to describe the sea ice albedo than features related to sea ice motion.

3.2 Physical interpretation of the best-performing equation

PySR selects the four best ranking features chosen by the SFS algorithm for the NN (see Sec. 3.1), namely h_{snow}, T_{0m}, h_{ice}, and T_{2m}, and neglects snowfall. This results in the following physically consistent equation with the lowest MSE

$$\alpha(h_{\text{snow}}, h_{\text{ice}}, T_{2m}, T_{0m}) = \frac{\tanh^2(\tilde{\text{p}}_{\text{snow}} h_{\text{snow}}^2 + \tilde{\text{p}}_{\text{ice}} h_{\text{ice}} + \tilde{\text{a}})}{\tilde{\text{b}} - \tanh(\tilde{\text{p}}_{T_{2m}} T_{2m} - \tilde{\text{p}}_{T_{0m}} T_{0m} + \tilde{\text{c}})}. \tag{4}$$

Equation 4 contains seven coefficients for which the optimised values are as follows

$$\{\tilde{\text{p}}_{\text{snow}}, \tilde{\text{p}}_{\text{ice}}, \tilde{\text{p}}_{T_{2m}}, \tilde{\text{p}}_{T_{0m}}, \tilde{\text{a}}, \tilde{\text{b}}, \tilde{\text{c}}\} = \{63.13\frac{1}{\text{m}^2}, 0.11\frac{1}{\text{m}}, 0.14\frac{1}{^\circ\text{C}}, 0.30\frac{1}{^\circ\text{C}}, 0.84, 2.19, 0.95\},$$

where $\tilde{\text{p}}_x$ denotes the weight of a feature x. The following subsections highlight the main physical findings discovered by Eq. 4 and which role the coefficients play.

3.2.1 High sensitivity to small variations in thin snow

In the numerator of Eq. 4, the squared hyperbolic tangent asymptotically approaches 1, causing changes in h_{snow} to have a greater impact on α than changes in h_{ice} for smaller values. For $x \to 0$ we have

$$\tanh(x) = x + O(x^3) \tag{5}$$

https://doi.org/10.5194/egusphere-2025-3556
Preprint. Discussion started: 8 October 2025

due to Taylor's theorem. Squaring Eq. 5 yields

$$\tanh^2(\tilde{\mathrm{p}}_{\mathrm{snow}} h_{\mathrm{snow}}^2 + \tilde{\mathrm{p}}_{\mathrm{ice}} h_{\mathrm{ice}} + \tilde{\mathrm{a}}) \approx (\tilde{\mathrm{p}}_{\mathrm{snow}} h_{\mathrm{snow}}^2 + \tilde{\mathrm{p}}_{\mathrm{ice}} h_{\mathrm{ice}} + \tilde{\mathrm{a}})^2 \tag{6}$$

for small values. As h_{snow} and h_{ice} increase, their impact on α diminishes due to the asymptotic nature of the hyperbolic tangent. Figure 3 illustrates how α changes rapidly within the first 20 cm of snow and then approaches an upper limit, whereas the relationship with h_{ice} is approximately linear with a small rate of change. The rapid increase of α within the first centimetres of snow aligns with known sea ice physics, as surface albedo is highly sensitive to small changes in thin snow, but becomes insensitive to differences in thicker snow and sea ice (e.g. Grenfell and Maykut, 1977; Perovich, 1996). Conversely, Perovich (1996) showed in a laboratory experiment that sea ice albedo also behaves asymptotically with increasing sea ice thickness. Here, due to the low weight value of h_{ice}, there is little difference in albedo response when increasing h_{ice}.

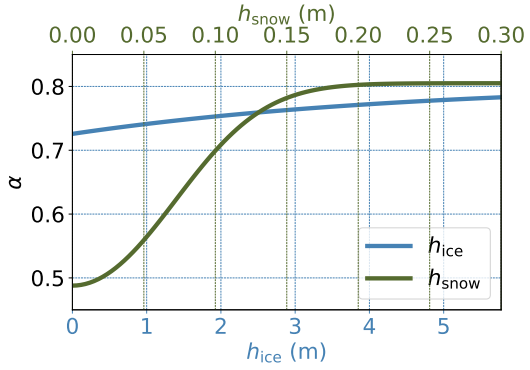

Figure 3. The response of Eq. 4 to varying snow depth (h_{snow}) and sea ice thickness (h_{ice}). While varying snow depth h_{snow} or sea ice thickness h_{ice}, the other features are fixed to their mean values during the validation period (2019–2020), shown in Table B1 (see Appendix B).

3.2.2 The weighted difference between the surface and 2 m air temperature as a seasonal proxy

Let ΔT^* be the weighted temperature difference that incorporates the weights:

$$\Delta T^* = \tilde{\mathrm{p}}_{T_{2\mathrm{m}}} T_{2\mathrm{m}} - \tilde{\mathrm{p}}_{T_{0\mathrm{m}}} T_{0\mathrm{m}} \tag{7}$$

PySR highlights that ΔT^* is more critical than the individual temperatures, with $T_{0\mathrm{m}}$ having double the impact on the denominator's hyperbolic tangent function in Eq. 4 compared to $T_{2\mathrm{m}}$, according to their weights. This supports the feature importance ranking (see Sec. 3.1), where $T_{0\mathrm{m}}$ is ranked higher than $T_{2\mathrm{m}}$, while both rank among the top four features despite their strong linear correlation of 0.92 (see Appendix A2). Although $T_{0\mathrm{m}}$ holds more weight than $T_{2\mathrm{m}}$, their importance remains interlinked due to this correlation, making their joint behaviour informative.

The hyperbolic tangent function in the denominator is strictly monotonically increasing, ranging between -1 and 1, approaching -1 as its input tends to negative infinity and 1 as it tends to positive infinity. Up to a constant, the ΔT^* controls both the

https://doi.org/10.5194/egusphere-2025-3556
Preprint. Discussion started: 8 October 2025

sign and the magnitude in the argument of tanh. Assuming $\tilde{p}_{T_{2m}}$ and $\tilde{p}_{T_{0m}}$ are always positive, if ΔT^* is positive, $\tanh(\Delta T^*)$ is pushed towards 1 and increases the overall value of $\alpha(h_{\text{snow}}, h_{\text{ice}}, T_{2m}, T_{0m})$. If ΔT^* is negative, $\tanh(\Delta T^*)$ is shifted towards -1, decreasing the overall value of $\alpha(h_{\text{snow}}, h_{\text{ice}}, T_{2m}, T_{0m})$.

Figures 4a and b illustrate how transforming the temperature difference $\Delta T = T_{2m} - T_{0m}$ to ΔT^* elucidates its relationship with observed α. At higher ΔT^*, α consistently remains high ($\alpha = 0.85$), unlike ΔT, where high α occurs between -15 °C and 15°C. Notably, when ΔT^* approaches zero, α decreases rapidly, an aspect which is not obvious with ΔT. Plotting the seasonal cycle in Fig. 4c, ΔT^* decreases steadily from winter, reaching a minimum of -0.19 in mid-July and then increases towards the fall, while ΔT shows two cycles with minima in May and mid-July. Consequently, ΔT^* serves as a seasonal proxy, where high ΔT^* corresponds to winter, early spring, and autumn, implying freezing and freeze-up conditions, whereas low ΔT^* aligns with late spring and summer, indicating melting conditions. The combined information of the sea ice surface and atmospheric conditions in ΔT^* can be interpreted as indicator for the transition between freezing and melting conditions.

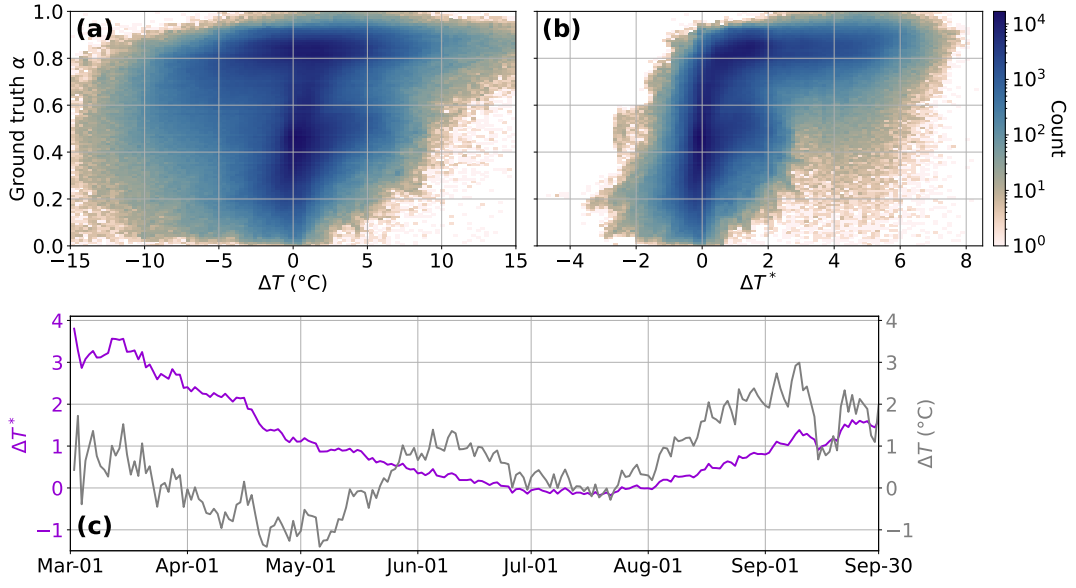

Figure 4. Comparison between the temperature difference $\Delta T = T_{2m} - T_{0m}$ and the weighted temperature difference $\Delta T^* = p_{\tilde{T}_{2m}} T_{2m} - p_{\tilde{T}_{0m}} T_{0m}$. Panel (a) and (b) show the density heat map for the observed sea ice albedo α and ΔT and ΔT^*, respectively, on a logarithmic scale. Panel (c) illustrates the seasonal cycle of observed ΔT and ΔT^* from March 1 to September 30 averaged from 2013 until 2020.

Since $\tanh(x)$ asymptotically approaches -1 and 1, the function becomes insensitive to large temperature differences, which is consistent with physical expectations, since extreme temperature differences do not significantly affect albedo once the ice is either fully melted or frozen.

https://doi.org/10.5194/egusphere-2025-3556
Preprint. Discussion started: 8 October 2025

3.2.3 Control of the upper and lower limit of sea ice albedo and the transition between melting and freezing conditions

In the following, we analyse the impact of the coefficients $\tilde{a}$, $\tilde{b}$ and $\tilde{c}$ on the sea ice albedo predictions. Equation 4 approaches its infimum (α_{inf}) when snow and ice are not present and when the denominator is maximised

$$\alpha_{\text{inf}} = \frac{\tanh^2(\tilde{a})}{\tilde{b}+1} \quad \text{for } \tilde{b} > -1. \tag{8}$$

Equation 8 highlights that $\tilde{a}$ controls the lower limit of the albedo, as depicted in Fig. 5a, which examines how α depends on h_{snow} with different $\tilde{a}$ values, while other features are set to their mean during validation (Table B1 in Appendix B). The analysis focuses solely on h_{snow} due to its greater influence on α compared to h_{ice} (see Sec. 3.2.1). The coefficient $\tilde{a}$ controls how quickly $\tanh^2(h_{\text{snow}}^2 + h_{\text{ice}})$ grows from its lower limit, as increasing $\tilde{a}$ shifts $h_{\text{snow}}^2 + h_{\text{ice}} + \tilde{a}$ to the right, making $\tanh^2(h_{\text{snow}}^2 + h_{\text{ice}} + \tilde{a})$ reach higher values more quickly. So, increasing $\tilde{a}$ raises the lower limit and makes the function grow faster from its minimum.

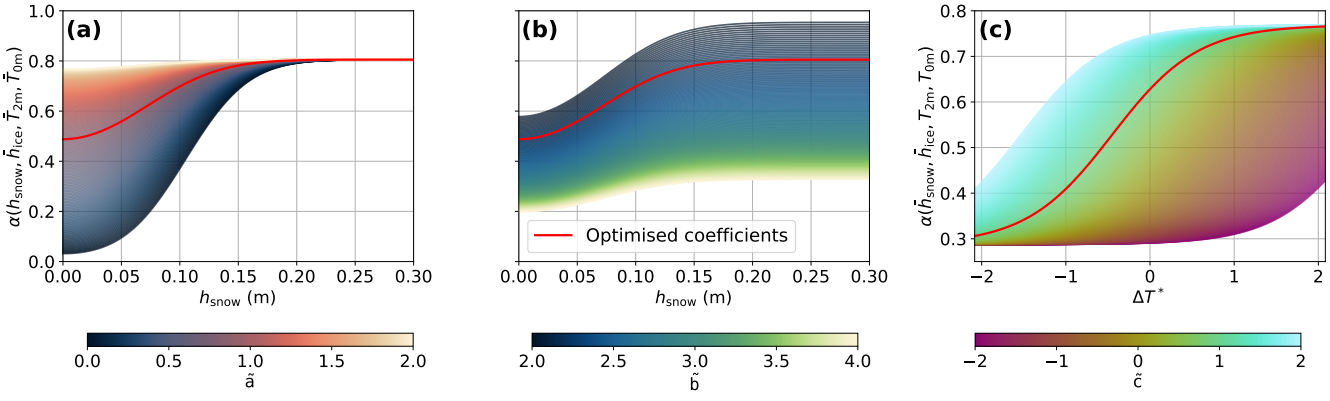

Figure 5. The impact of the coefficients $\tilde{a}$, $\tilde{b}$ and $\tilde{c}$ on the functional behaviour of Eq. 4. Panels (a) and (b) illustrate the dependency of sea ice albedo (α) on snow depth (h_{snow}) with varying $\tilde{a}$ and $\tilde{b}$, respectively. Panel (c) demonstrates the response on the difference between 2m temperature ($T_{2\text{m}}$) and surface temperature ($T_{0\text{m}}$) with varying $\tilde{c}$. The other coefficients are kept fixed at their optimal values and the other features at their mean values during the validation period (2019–2020) denoted with bar overhead (Table B1 in Appendix B). The red line indicates Eq. 4 with the optimised coefficient values (see Sec. 3.2).

Equation 4 approaches its supremum (α_{sup}) when the numerator is maximised and the denominator is minimised, while $\tilde{b}$ is controlling the upper limit of the albedo

$$\alpha_{\text{sup}} = \frac{1}{\tilde{b}-1} \quad \text{for } \tilde{b} > 1. \tag{9}$$

As $\tilde{b}$ increases, the upper limit decreases and vice versa (Fig.5b). Since the denominator must be greater than 1 to keep α within its physical range (0 to 1), $\tilde{b}$ should be greater than 2 to ensure physical consistency. Plugging in the optimised coefficients, we get $\alpha_{inf} = 0.15$ and $\alpha_{sup} = 0.84$.

https://doi.org/10.5194/egusphere-2025-3556
Preprint. Discussion started: 8 October 2025

The coefficient $\tilde{c}$ shifts the response curve of Eq. 4, thereby modulating the transition between freezing and melting conditions (Fig. 5c). Decreasing $\tilde{c}$ shifts the response curve to the right, meaning that melting conditions already occur at higher ΔT^*, and vice versa, suggesting the presence of other sources (e.g., oceanic heat) influencing sea ice optical properties, which are not accounted for in Eq. 4.

4 Comparison of Eq. 4 with PW79 and baseline models

4.1 Balancing model error and complexity

Figure 6 presents the five best-performing equations in terms of MSE discovered by PySR (see Appendix C for the equations ranked second to fifth) and baseline models, including polynomials and NNs, on an error-complexity plane (see Sec. 2.2.5). Optimising PW79 using the Nelder-Mead method reduces the MSE from 0.08 to 0.03. Despite this improvement, all models outperform the tuned PW79.

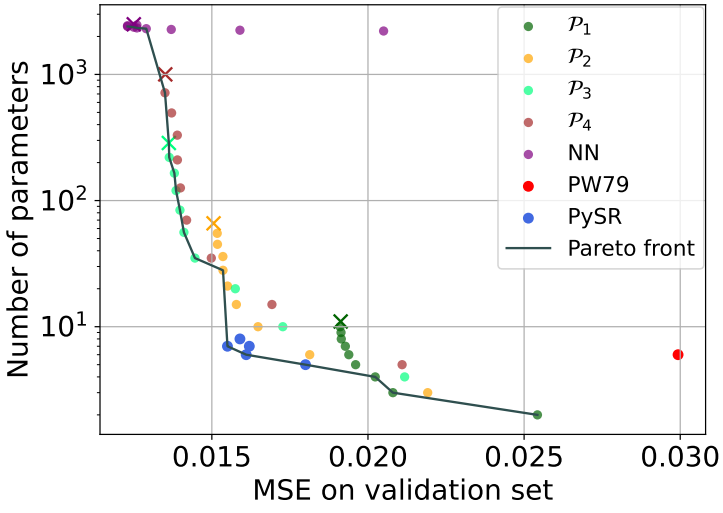

Figure 6. Error-complexity plane. The mean squared error (MSE) on the validation set is on the x-axis, while model complexity, defined as the number of tunable parameters, is plotted on a logarithmic y-axis. We compare the five best-performing physically consistent equations derived with PySR with the tuned FESIM parametrisation and with baseline models of different types: polynomials of different degrees $\mathcal{P}_{1-4}$, and neural networks (NNs). For each model type, models with an increasing number of features, chosen by the sequential feature selection (SFS) algorithm, are evaluated. With the exception of the NNs, those can be read from right to left with increasing number of features. Models with all ten features are marked with a cross. The Pareto front traces out the best models for a given maximum complexity.

Notably, increasing the polynomial degree from one to two yields a significant reduction in MSE of approximately 0.005. However, further increasing the degree to three or four does not result in substantial performance gains, indicating that model complexity beyond this point does not lead to significant improvements. Moreover, increasing feature dimensionality leads to

https://doi.org/10.5194/egusphere-2025-3556
Preprint. Discussion started: 8 October 2025

a convergence of model performance within each model family, typically after adding the fourth or fifth feature. This suggests that the first four or five features chosen by the SFS algorithm represent the key features that govern albedo, while the remaining features are redundant, contributing less marginal information or introducing noise.

The full-set NN exhibits slight overfitting (MSE $= 0.0125$), since it is less skilful than the 7-feature NN (ΔMSE $= 0.0002$). Thus, we find that sparsity can help the NN to generalise. Interestingly, polynomials and NNs show similar performance, with polynomials requiring additional features to match the accuracy of NNs. For instance, comparable performance is observed in models like 1-feature NN and 3-feature $\mathcal{P}_1$, and 2-feature NN and 4-feature $\mathcal{P}_2$. The comparable model performances suggest that simpler polynomial models are sufficient to capture the underlying patterns between the features and albedo, and are as effective as NNs, which may be overly complex for this problem. Furthermore, the need for additional features in polynomials may be beneficial, as it can help to compensate structural uncertainty in the parametrisation.

4.2 Sea ice albedo distribution

Figure 7a compares the sea ice albedo distributions during the validation period between the ground truth and model predictions, all illustrated within the physical range between 0 and 1. The model predictions are: Equation 4, 4-feature $\mathcal{P}_3$ (Eq. D1 in Appendix D), and 4-feature NN to compare models with the same number of features. The Hellinger distance measures the similarity between two discrete univariate probability distributions P and Q

$$H(P,Q) \stackrel{\text{def}}{=} \frac{1}{\sqrt{2}} ||\sqrt{P} - \sqrt{Q}||_2. \tag{10}$$

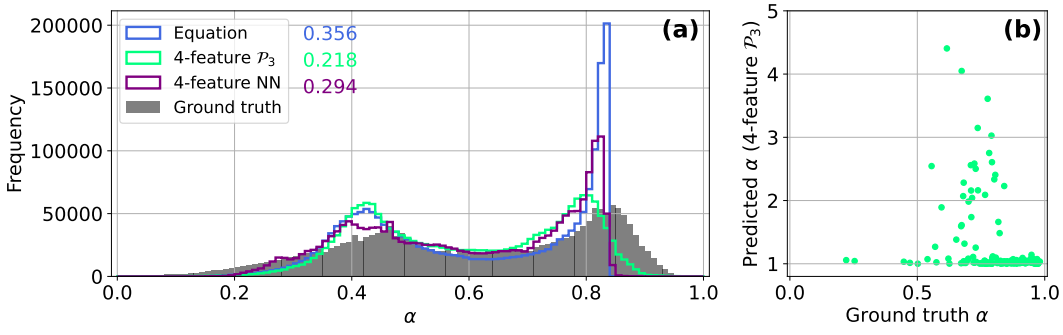

Figure 7. Comparison of the sea ice albedo distributions during the validation period (2019–2020) between the VIIRS product (Key et al., 2001, 2016) as ground truth and the predictions from the best-performing models in each model class in terms of MSE. Panel (a) illustrates the distribution of the ground truth alongside predictions from the best-performing equation (Eq. 4), the 4-feature polynomial of degree three $\mathcal{P}_3$, and the 4-feature neural network (NN), all within the physical range between 0 and 1. The Hellinger distance for each model is shown next to the legend in their respective colors. Panel (b) shows predicted albedo values falling outside the physical range for the polynomial of degree three with four features, plotted against the observed sea ice albedo.

The three model predictions exhibit a bimodal distribution similar to the ground truth (with peaks at 0.46 and 0.84). Among the models, 4-feature $\mathcal{P}_3$ shows the greatest similarity to the ground truth, with a Hellinger distance of 0.218 and MSE of

https://doi.org/10.5194/egusphere-2025-3556
Preprint. Discussion started: 8 October 2025

0.0145. This is followed by the 4-feature NN, with a Hellinger distance of 0.294 and MSE of 0.0133, and Eq. 4, with Hellinger distance of 0.356 and MSE of 0.0156. However, some of the predicted sea ice albedo values from 4-feature $\mathcal{P}_3$ fall outside the physical range of 0 and 1, as illustrated in Fig. 7b, violating the first PC. Additionally, none of the models fully capture the long tail of the ground truth towards higher albedo values. Instead, both 4-feature NN and Eq. 4 demonstrate a notable peak at higher albedo values (0.82 and 0.83, respectively), with Eq. 4 having an upper limit for sea ice albedo at 0.83. At the lower end of the albedo scale, the 4-feature NN best captures the long tail, although all model peaks at lower albedo values are more shifted compared to the ground truth: 0.42 for the 4-feature $\mathcal{P}_3$, 0.39 for the 4-feature NN, and 0.42 for Eq. 4.

During training, we do not account for uncertainties associated with various satellite products. For the VIIRS product, the overall uncertainty for albedo retrieval is 0.1, and for surface temperature, it is 1.98 K, based on RMSE comparisons with in-situ measurements from the SHEBA campaign (Key et al., 2001, 2016). Light et al. (2022) assessed the albedo of eight individual sea ice surface types of sea ice based on field measurements from the MOSAiC expedition, finding that early autumn snow exhibits the highest albedo values between 0.8 and 0.9, while dark ponds have the lowest albedo values between 0.12 and 0.25. Thus, we conclude that the long tails of the ground truth albedo, values below 0.12 and above 0.9, are likely due to measurement, data processing, and retrieval errors. Moreover, our dataset has a spatial resolution of 25 km, which covers a variety of sea ice surface types, providing spatially averaged albedo values. In contrast, Light et al. (2022) reports highly localised albedo values for each surface type. Based on these considerations, we conclude that the upper albedo limit of Eq. 4 is physically reasonable, given that the ground truth is noisy and reflects average albedo over a large area.

4.3 Spatial maps of sea ice albedo

Figure 8 illustrates the sea ice albedo exemplarily for May 23rd, 2020, with ground truth (Fig. 8a), computed with the tuned PW79 (Fig. 8b), and Eq. 4 (Fig. 8c). Figures 8d-e depict deviations from the observed albedo. The tuned PW79 demonstrates two areas distinguishing between high and low albedo zones due to its constant albedo values representing surface types, namely snow-covered ice ($\alpha = 0.66$), and melting snow ($\alpha = 0.40$). As PW79 is not a smooth function, PW79 causes a sharp border between the two surface types. Conversely, the spatial variability of the observed albedo is better captured with Eq. 4, reducing the MSE by about a half (0.0156) compared to the tuned PW79 (0.0300). Biases remain in the Hudson Bay and along the sea ice edges, but are much reduced in the Central Arctic.

4.4 Seasonal cycle of sea ice albedo

Figure 9 presents the seasonal albedo cycle of the ground truth, Eq. 4, and tuned and untuned PW79 for the period March to September, averaged from 2013 to 2020. The untuned PW79, unlike the other parametrisations, maintains a constant albedo at about 0.81, showing no seasonality. In contrast, the other three datasets display strong seasonality, with maximum sea ice albedo occurring during the winter period between March and April, followed by a steady decrease during the melting period between May and July, where it reaches its minimum. Equation 4 demonstrates a strong agreement with the ground truth, achieving an R^2 score of 0.94, whereas both untuned and tuned PW79 reach 0.57. During the winter period, the tuned PW79 starts with much lower albedo values around 0.66 compared to the ground truth and Eq. 4, which display sea ice albedo of

https://doi.org/10.5194/egusphere-2025-3556
Preprint. Discussion started: 8 October 2025

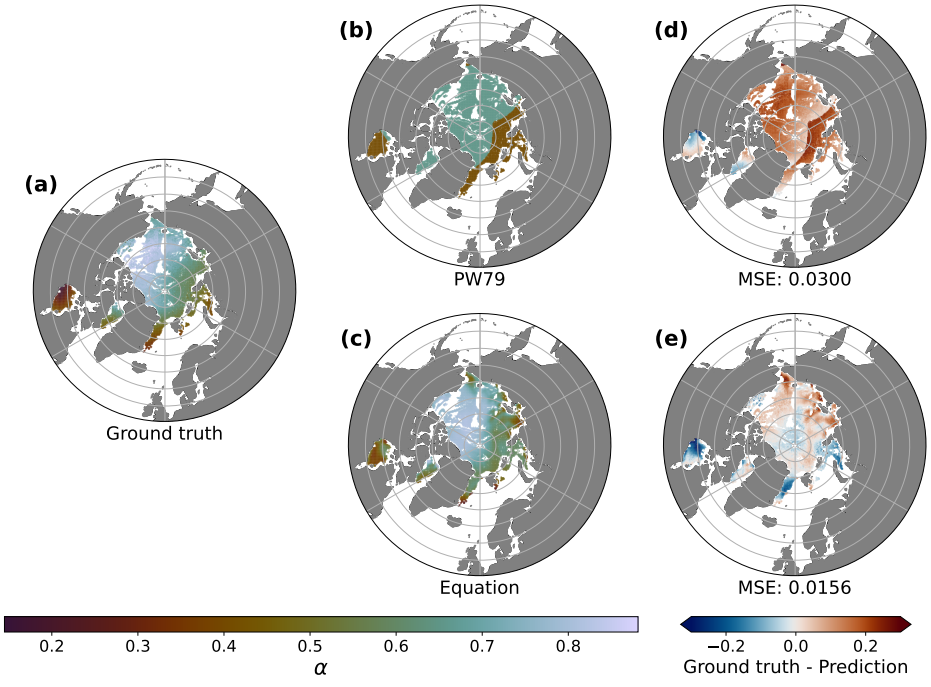

Figure 8. Comparison between (a) the sea ice albedo observed via the VIIRS satellite instrument (Key et al., 2001, 2016) as ground truth, (b) the tuned FESIM parametrisation, and (c) the best-performing equation (Eq. 4) for May 23rd, 2020. The deviations to the ground truth are illustrated in panel (d) for PW79 and panel (e) for Eq. 4.

similar magnitude of around 0.77. While the tuned PW79 reaches its minimum in July at 0.42, Eq. 4 reveals its minimum at 0.39, which is closer to the ground truth with 0.27. During the freeze-up period in August and September, the tuned PW79 demonstrates a rapid increase in sea ice albedo, similar in magnitude to the winter period. In contrast, the ground truth and Eq. 4 depict a more gradual increase, with sea ice albedo not recovering as rapidly to winter magnitude in August.

While Eq. 4 remains gradually increasing in September, the ground truth shows a decrease of sea ice albedo, which contradicts the expected freeze-up behaviour of Arctic sea ice (Pistone et al., 2014; Light et al., 2022). Peng et al. (2018) showed that the quality and accuracy of the VIIRS albedo product decrease with increasing solar zenith angle in September. Despite being trained on the ground truth, Eq. 4 provides a more physically reasonable prediction for September, likely due to the sparse observational data available for that month, as reduced sunlight over the pole limits September data availability (see Appendix E), resulting in less weight being given to these observations during training. Therefore, PySR relies more heavily on the complete data from March to August (see Sec. Fig. 2). As a result, PySR implicitly captures seasonal patterns, particularly temperature-driven trends (see Sec. 3.2.2), which extend naturally into September. In doing so, Eq. 4 effectively corrects for potential measurement artefacts in the September data by leveraging the functional relationships between ΔT^* and sea ice albedo learnt from better sampled months.

https://doi.org/10.5194/egusphere-2025-3556
Preprint. Discussion started: 8 October 2025

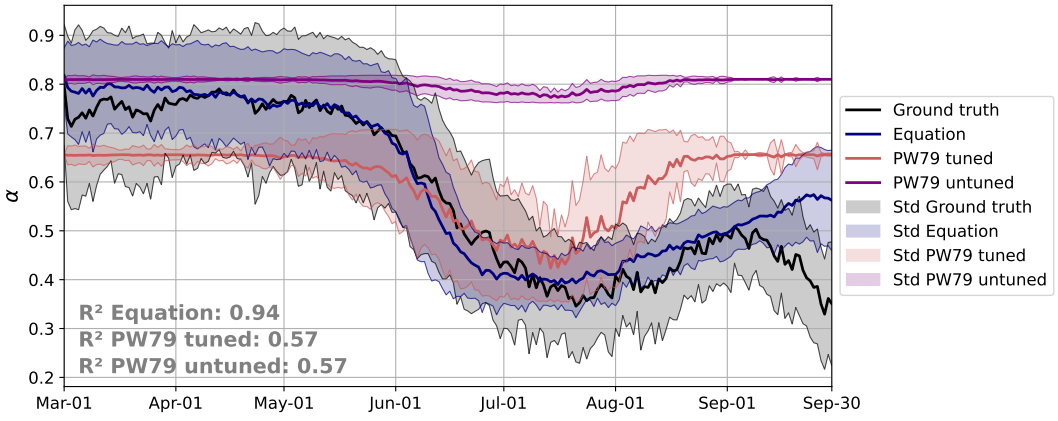

Figure 9. Seasonal sea ice albedo cycle from March 1 to September 30 averaged from 2013 until 2020 observed via the VIIRS satellite instrument (Key et al., 2001, 2016) as ground truth, and computed with the best-performing equation (Eq. 4), and the sea ice albedo parametrisation by Parkinson and Washington (1979), here reffered to as PW79. The untuned PW79 corresponds to the standard configuration of the Finite-Element Sea Ice Model (FESIM; Danilov et al., 2015), while for a fair data-driven comparison, PW79 is tuned to the training set, including data from 2013 to 2018, using the Nelder-Mead method (Nelder and Mead, 1965).

Both tuned and untuned PW79 exhibit very low standard deviations during the winter period and September, with higher values around 0.13 during the melting season for the tuned PW79. Conversely, the ground truth shows high standard deviations with a maximum of 0.19, which are attributed to the spatial variability of sea ice albedo and measurement, data processing, and retrieval errors as already discussed in Sec. 4.2. Equation 4 reveals lower standard deviations with a maximum of 0.16, potentially eliminating errors, and are attributed solely to the spatial variability of the albedo. The low standard deviations in the tuned and untuned PW79 stem from its simplistic nature, relying on constant albedo values based on snow cover and surface temperature, where each constant represents a sea ice surface type. This results in PW79 perceiving the sea ice as highly uniform during the winter and September, whereas the tuned PW79 captures more variability during the melting season.

Overall, Eq. 4 presents a clear improvement over PW79, aligning with observed sea ice albedo variations by capturing both the seasonal progression and its magnitude. The untuned PW79 does not capture the observed albedo seasonality, maintaining a high value of 0.81 year-round. It should be noted, that the sea ice albedo is calculated for each of these methods with observed melting conditions, which could differ from the conditions in FESIM.

Although the tuned PW79 better captures sea ice albedo seasonality, it significantly deviates in magnitude, inaccurately reflecting albedo changes and showing an earlier, quicker freeze-up than the ground truth. Both the ground truth and Eq. 4 align with previous field campaigns from SHEBA (Perovich et al., 2002) and MOSAiC (Light et al., 2022), identifying five phases of Arctic sea ice: dry snow (March-Aril), melting snow (May), pond formation (June), pond development (July), and freeze-up (August-September). It is noticeable that these studies were based on highly localised measurements, whereas this study investigates spatially averaged data over a 25 km resolution.

https://doi.org/10.5194/egusphere-2025-3556
Preprint. Discussion started: 8 October 2025

5 Regional and monthly optimisation of Eq. 4

5.1 Comparison between the optimisation strategies

Figure 8e reveals regional differences in model performance for Eq. 4, suggesting that the global optimisation approach on the entire training set is not able to capture the underlying patterns uniformly across all regions. This finding motivates us to explore spatial and temporal variations in model performance by conducting optimisations on regional and monthly subsets. As Eq. 4 provides physically meaningful coefficients, as demonstrated in Sec. 3.2.3, we are able to gain insights into the underlying physical mechanisms governing model performance. In contrast, optimising NNs on subsets would not offer the same level of interpretability due to their inherent black-box nature. To ensure consistency across all subset optimisations, we divide our training set into monthly and regional subsets, utilising 20,000 data samples for each region and 10^5 data points for each month.

Both monthly (MSE $= 0.0122$) and regional (MSE $= 0.0117$) optimisation strategies outperform global optimisation (MSE $= 0.0156$) in terms of reducing overall MSE (Fig. 10a-c) albeit making the coefficients depend on the region or month greatly increases the complexity of Eq. 4. This improvement is likely due to the ability of Eq. 4 to capture regional and monthly variations in the data. The regional optimisation approach leads to significant reductions in MSE for certain regions, such as the Barents Sea (from 0.0460 to 0.0220), Kara Sea (from 0.0409 to 0.0263), and East Greenland Sea (from 0.0335 to 0.0148) (Fig. 10e). However, these regions, which border the North Atlantic, continue to exhibit high MSEs across all optimisation strategies, suggesting that they may be influenced by physical processes not well-represented by Eq. 4, such as Atlantic Oceanic heat transport or strong winds prevailing in these regions (Screen and Simmonds, 2010; Årthun et al., 2012; Liu et al., 2024). Another potential reason is that the underlying physics operate on a time scale smaller than our data, which are on a daily basis due to the temporal resolution of the satellite data.

In terms of the magnitude of improvement, regional optimisation yields higher proportional improvements compared to monthly optimisation (Fig. 10d-e). The greatest proportional improvements in the reduction of MSE are observed for the Chuckshi Sea with regional optimisation (75%), September with monthly optimisation (69%), and the Beaufort Sea (59%). However, the Central Arctic shows little improvement with regional optimisation, likely due to its dominant representation in the dataset (64% of the entire dataset). As a result, the global optimisation is already greatly influenced by the Central Arctic data, and the optimal coefficients are likely biased towards this region, leaving little room for improvement with regional optimisation.

One limitation of the regional optimisation approach is that it produces sharp borders in the error map (Fig. 10c), reflecting the regional focus of the optimisation process, which leads to a lack of a smooth error transitions between regions. Additionally, some instances of overfitting are observed, where regional or monthly optimisation results in high MSE values compared to global optimisation. For example, the MSE of July with monthly optimisation (0.0088) is higher than with global optimisation (0.0080), and similar patterns are seen for Hudson Bay with regional optimisation (0.0138 vs. 0.00116), and Laptev Sea with regional optimisation (0.0185 vs. 0.0172).

https://doi.org/10.5194/egusphere-2025-3556
Preprint. Discussion started: 8 October 2025

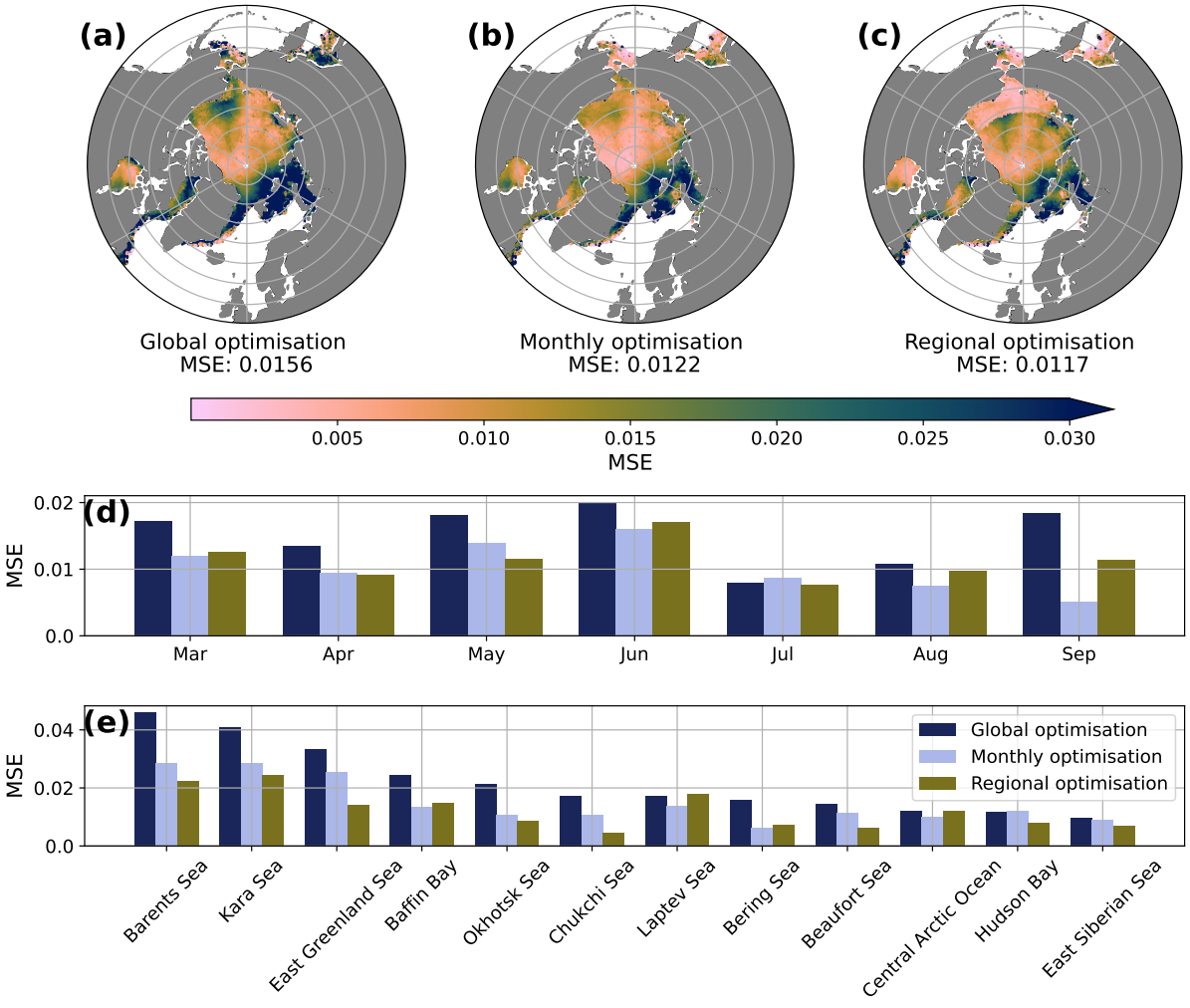

Figure 10. Monthly and regional analysis. Panels (a), (b) and (c) illustrate the mean squared error on the validation set (MSE) for each grid cell for the global, monthly, and regional optimisation, respectively. Panels (d) and (e) show the MSE for each month and region, respectively, when fine-tuning Eq. 4 globally (brown), on each month (green), and on each region (red).

5.2 Case study: Barents Sea

The optimised coefficients for each region and month resulting in the analysis in Sec. 5.1 are displayed in Appendix F and Appendix G, respectively. Physical interpretation of each region and month goes beyond the scope of this study. Instead, we focus on the Barents Sea as a case study. This region exhibits the highest MSE from global optimisation and significant improvement with regional optimisation. For a direct comparison, the coefficients are standardised to their unitless form (Table 3).

https://doi.org/10.5194/egusphere-2025-3556
Preprint. Discussion started: 8 October 2025

Table 3. Unitless coefficients, divided by the respective standard deviations of the training set (2013–2018), for the whole dataset representing the entire pan-Arctic region and Barents Sea, optimised on the validation period (2019–2020).

	$\tilde{p}_{\text{snow,std}}$	$\tilde{p}_{\text{ice,std}}$	$\tilde{p}_{T_{2m},\text{std}}$	$\tilde{p}_{T_{0m},\text{std}}$	$\tilde{a}$	$\tilde{b}$	$\tilde{c}$
pan-Arctic	0.85	0.09	0.99	2.16	0.84	2.19	0.95
Barents Sea	0.03	0.64	0.34	1.89	0.34	2.29	-0.04

In the Barents Sea, the effect of h_{snow} becomes significantly smaller ($\tilde{p}_{\text{snow, std}} = 0.03$) compared to the pan-Arctic region ($\tilde{p}_{\text{snow}} = 0.85$), while h_{ice} becomes more important ($\tilde{p}_{\text{ice,std}} = 0.64$) than in the pan-Arctic region ($\tilde{p}_{\text{ice,std}} = 0.09$). These differences reflect the distinct physical conditions in these regions. The Barents Sea experiences high seasonality, with thin sea ice prevalent and little to no snow present, compared to the whole pan-Arctic region (Smedsrud et al., 2013). Consequently, variations in thin sea ice play a more significant role in sea ice albedo in the Barents Sea, whereas variations in thin snow influence sea ice albedo in the pan-Arctic region.

In both cases, $T_{0\text{m}}$ has the highest weight (of around 2). However, $T_{2\text{m}}$ is less significant in the Barents Sea ($\tilde{p}_{T_{2\text{m}},\text{std}} = 0.34$) than in the pan-Arctic region ($\tilde{p}_{T_{2\text{m}},\text{std}} = 0.99$). In the pan-Arctic region ($\tilde{c} = 0.95$), smaller ΔT^* are required to trigger melting, while in the Barents Sea, the lower value of $\tilde{c} = -0.04$ triggers melting conditions already at higher ΔT^*. The shift of the transition to higher ΔT^* implies other heat sources affecting sea ice optical properties which are not considered in Eq. 4, as already discussed in 5.1.

Our findings indicate that the pan-Arctic region represents a stable ice regime, in which snow and small ΔT^* modulate sea ice albedo, while the Barents Sea represents a fragile ice regime, where ice properties and temperatures already at higher ΔT^* regulate albedo sensitivity. The Barents Sea is one of the most rapidly changing regions, becoming ice-free in summer and contributing to approximately one-quarter of the Arctic sea ice loss in winter. This change is associated with surface warming in the Gulf Stream and the increase of the Atlantic oceanic heat transport passing the Barents Sea Opening (Yamagami et al., 2022; Årthun et al., 2012; Smedsrud et al., 2013; Stroeve and Notz, 2018).

6 Conclusions

In this study, we derived an interpretable, physically consistent equation for sea ice albedo through the integration of several multi-year satellite and reanalyses data covering the pan-Arctic region and the application of various machine learning techniques, including NNs, SFS, and symbolic regression with PySR. Our best-performing data-driven equation (Eq. 4) combines two mechanisms that critically impact sea ice albedo: high sensitivity to small changes in thin snow, and the temperature difference between the sea ice surface and 2 m air, weighted in a way such as to reflect the current season. While the PW79 sea ice albedo parametrisation only uses the surface temperature as a proxy to define freezing and melting conditions, our equation shows that a weighted temperature difference between the surface and the air at 2 m better quantifies the rate of change in sea ice albedo.

https://doi.org/10.5194/egusphere-2025-3556
Preprint. Discussion started: 8 October 2025

The error-complexity graph demonstrates that NNs are overly complex and that lower-complexity models are sufficient to achieve comparable performance. Equation 4 significantly outperforms PW79, reducing the MSE on the observational validation set by half and improving the representation of the spatial variability and seasonal cycle of sea ice albedo. Moreover, Eq. 4 sets lower and upper limits for sea ice albedo due to the functional behaviour of the hyperbolic tangent, that are physically plausible and yield realistic sea ice albedo values. By adapting the coefficients of Eq. 4 to subsets of the dataset, it demonstrates its flexibility in regional and monthly assessments, allowing for a more in-depth analysis of the underlying physics within each subset as the optimised coefficients can be directly interpreted.

One methodological constraint in our approach is the selection of features that are available on a daily basis across the entire pan-Arctic region and are also represented in FESIM and FESOM, our primary target ocean-sea ice models. This deliberate feature selection ensures compatibility with our modelling objectives, but overlooks other relevant factors that may substantially impact sea ice albedo. This includes explicit melt pond information, which is known to significantly reduce sea ice albedo, as demonstrated in numerous studies (e.g. Perovich et al., 2002; Webster et al., 2022; Niehaus et al., 2024). Although a coupled FESOM-Icepack version was developed (Zampieri et al., 2021; Hunke et al., 2023), which explicitly resolves melt ponds, computational constraints for including Icepack in the Alfred Wegener Institute Climate Model (AWI-CM3; Streffing et al., 2022) led us to prioritise FESIM's simpler sea ice thermodynamics formulation with the PW79 parametrisation. Furthermore, snow grain size also substantially determines sea ice/snow albedo (Perovich, 1996; Perovich et al., 2002), but there is no data available on a daily, pan-Arctic scale. Nevertheless, since the objective of this study is to capture large-scale patterns at $25 \times 25\,\mathrm{km}^2$ resolution, Eq. 4 sufficiently explains the variance in observed sea ice albedo, indicating that small-scale features may have a limited marginal effect at this scale.

Another consideration of our approach is that this study aimed to minimise global MSE on the validation set, with the Central Arctic dominating the dataset spatially and temporally. As this mirrors real-world conditions, other subregions are underrepresented in our dataset. Consequently, the ranking resulting from SFS and Eq. 4 is likely optimised for the Central Arctic, as evident from monthly and regional differences in MSE. To balance the data, dominant subregions or months could be downsampled, which results in a more diverse training set, but this would most likely lead to a higher MSE overall. In future studies, focused on regional-scale modelling, we recommend to optimise Eq. 4 to the region of interest as we did exemplarily in Sec. 5.

This study demonstrates the first use of interpretable ML in sea ice modelling to foster trust and transparency in the Earth system community. Bridging a gap between the ML and the Earth system science community, we leveraged interpretable ML techniques to gain a deeper understanding of the physical mechanisms driving sea ice albedo. Our approach contributes to the growing body of research that establishes ML as a valuable tool in Earth system science, with applications in data assimilation, numerical weather predictions, and climate emulators.

https://doi.org/10.5194/egusphere-2025-3556
Preprint. Discussion started: 8 October 2025

Code and data availability. The data sources of the datasets forming the basis of this paper are given in the references provided throughout the text and are summarised in Table 1. The code will be published under https://github.com/EyringMLClimateGroup/atmojo25tc_equationdiscovery_seaicealbedo.

Appendix A: Correlation matrices

A1 Comparison between observational and reanalysis data for March and April (2013–2020)

Satellite instruments are not able to reliably retrieve h_{snow} and h_{ice} during the summer months (May-September) due to the presence of melt ponds which distort the signal coming from the snow and sea ice (Rostosky et al., 2018; Ricker et al., 2017). To fill the data gaps, reanalysis data seem to be useful as they provide spatio-temporal coverage assimilated with observational data. To assess whether filling data gaps with reanalysis data is appropriate, Fig. A1 compares the correlation matrices of the datasets for the period March until mid April from 2013 to 2020 with h_{snow} and h_{ice} retrieved from satellite observations (Table 1, Fig. A1(a)), and from the Arctic Ocean Physics Reanalysis *TOPAZ4b* (Fig. A1(b)). The correlation matrices of both datasets look similar as the linear correlations between all features have the same signs of comparable magnitude, which justifies using *TOPAZ4b* for h_{snow} and h_{ice} to fill the gaps during the summer months.

A2 Correlation matrix of final dataset (from March until September, 2013–2020)

Figure A2 presents the correlation matrix of the preprocessed dataset from several data products as described in Table 1, consisting of data from March until September from 2013 to 2020.

Appendix B: Mean values of the features during the validation period (2019–2020)

Table B1 shows the mean values of the features h_{snow}, h_{ice}, $T_{0\text{m}}$ and $T_{2\text{m}}$ during the validation period (2019–2020).

Table B1. Mean values of the features during the validation period (2019–2020).

Feature	Mean values
$\bar{h}_{\text{snow}}$	0.12 m
$\bar{h}_{\text{ice}}$	1.80 m
$\bar{T}_{0\text{m}}$	-5.49 °C
$\bar{T}_{2\text{m}}$	-5.38 °C

Appendix C: Selected Symbolic Regression Fits

The best-performing equations discovered by PySR are listed that satisfy the physical constraints (see Sec. 2.2.4) and showcased in Fig. 6, ranked in increasing MSE order with the MSE/number of parameters in brackets. Equations 1, 2, and 3 are

https://doi.org/10.5194/egusphere-2025-3556
Preprint. Discussion started: 8 October 2025

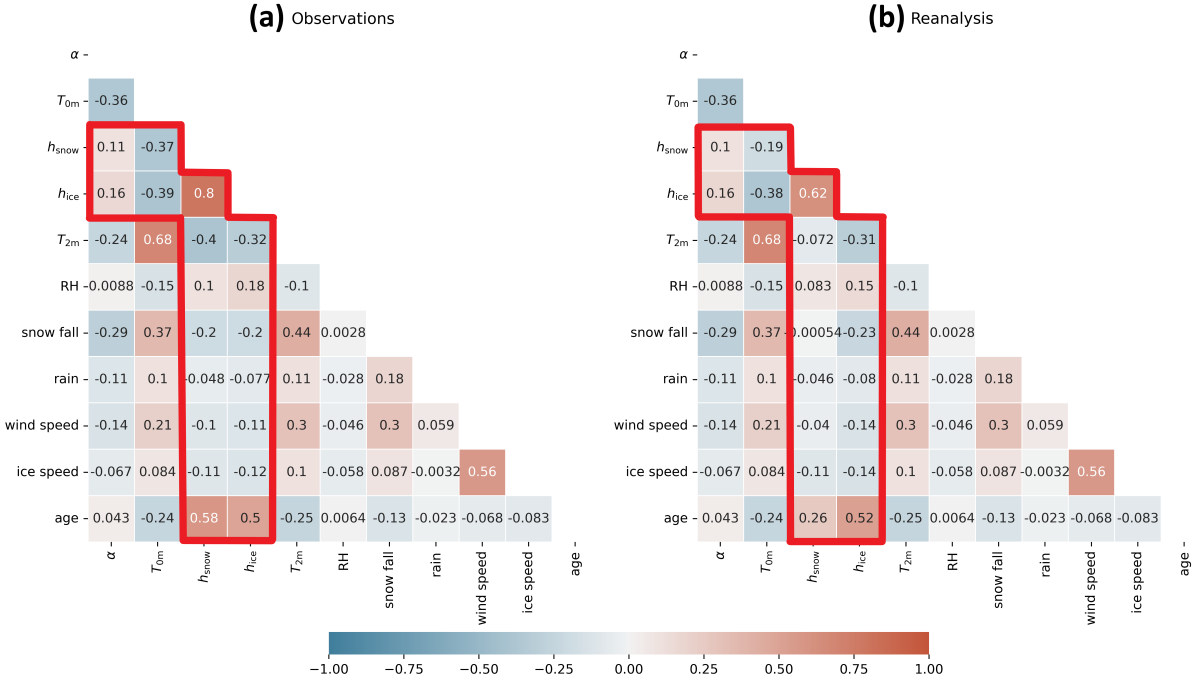

Figure A1. Correlation matrices for comparing snow (h_{snow}) and sea ice thickness (h_{ice}) data retrieved from (a) the satellite observations AMSR2 (Rostosky et al., 2018) and CS2SMOS (Ricker et al., 2017), respectively, and (b) Arctic Ocean Physics Reanalysis *TOPAZ4b* (European Union-Copernicus Marine Service, 2020) from March until mid April (2013–2020). The red marking indicates the comparing linear correlations between satellite observations and reanalysis.

optimised with the Nelder-Mead solver, and equations 4 and 5 with the BFGS-solver. Note that the equations are shown in their standardised form following Eq.1. Equations 1, 3 and 5 are Pareto-optimal, which are denoted in bold:

1. **[0.155/7]**: $\alpha(h_{\text{ice}}, h_{\text{snow}}, T_{2\text{m}}, T_{0\text{m}}) = \frac{\tanh^2(0.09h_{\text{ice}}+0.85h_{\text{snow}}^2+0.84)}{2.19-\tanh(0.98T_{2\text{m}}-2.17T_{0\text{m}}+0.93)}$
2. [0.0159/8]: $\alpha(h_{\text{ice}}, h_{\text{snow}}, T_{0\text{m}}) = -0.92 + \frac{\sqrt{0.32+(0.83T_{0\text{m}}+0.35)^2}}{1.05h_{\text{ice}}\sqrt{h_{\text{snow}}}+1.52(1.04h_{\text{snow}}^2T_{0\text{m}}^2+1.18)^2}$
3. **[0.0161/6]**: $\alpha(h_{\text{ice}}, h_{\text{snow}}, T_{0\text{m}}) = 0.83\left(1+\frac{-0.43}{1.74h_{\text{snow}}^4T_{0\text{m}}^4+\sqrt{2.01h_{\text{ice}}^2h_{\text{snow}}+|-0.95T_{0\text{m}}+1.70|}}\right)^2$
4. [0.0162/7]: $\alpha(h_{\text{ice}}, h_{\text{snow}}, T_{0\text{m}}) = 0.84\left(1+\frac{-0.66}{0.83h_{\text{ice}}\sqrt{h_{\text{snow}}}+(1.18h_{\text{snow}}^2T_{0\text{m}}-1)^2+(-0.71T_{0\text{m}}^2-0.68T_{0\text{m}}+0.97)^2}\right)^2$
5. **[0.0180/5]**: $\alpha(h_{\text{ice}}, h_{\text{snow}}, T_{0\text{m}}) = 0.84\left(1+\frac{-0.79}{2.04\sqrt{h_{snow}}+(1.24h_{\text{snow}}^2T_{0\text{m}}-1.55)^2}\right)^2$

https://doi.org/10.5194/egusphere-2025-3556
Preprint. Discussion started: 8 October 2025

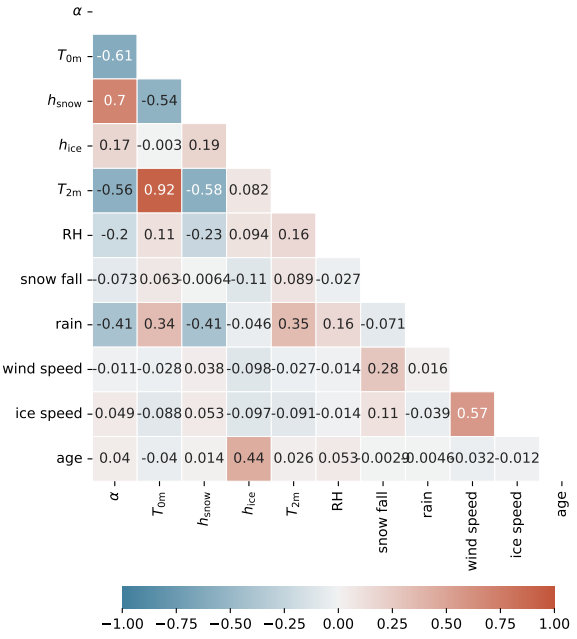

Figure A2. Correlation matrix of preprocessed dataset from several data products (Table 1. From March until mid April, h_{snow} and h_{ice} are retrieved from satellite observations (Rostosky et al., 2018; Ricker et al., 2017). The data gaps from mid April until September are filled with the Arctic Ocean Physics Reanalysis *TOPAZ4b* (European Union-Copernicus Marine Service, 2020) as described in Sec. 2.1.2.

Appendix D: 4-feature polynomial of degree three $\mathcal{P}_3$

Equation D1 represents the 4-feature polynomial of degree three $\mathcal{P}_3$ for which the distribution of predicted sea ice albedo during the validation period (2019–2020) is shown in Fig. 7. $\mathcal{P}_3$ consists of the features $h_{\text{snow}}, T_{0\text{m}}, T_{2\text{m}}, h_{\text{ice}}$. Note that Eq. D1 is shown in its standardised form following 1.

$$
\begin{aligned}
\alpha(h_{\text{snow}}, T_{0\text{m}}, T_{2\text{m}}, h_{\text{ice}}) = {} & 0.2266 + 0.3046\,h_{\text{snow}} - 0.1694\,T_{0\text{m}} + 0.0129\,T_{2\text{m}} + 0.1331\,h_{\text{ice}} - 0.1385\,h_{\text{snow}}^2 \\
& - 0.1267\,h_{\text{snow}}T_{0\text{m}} - 0.0212\,h_{\text{snow}}T_{2\text{m}} + 0.0159\,h_{\text{snow}}h_{\text{ice}} - 0.0928\,T_{0\text{m}}^2 + 0.0081\,T_{0\text{m}}T_{2\text{m}} \\
& + 0.0116\,T_{0\text{m}}h_{\text{ice}} + 0.0254\,T_{2\text{m}}^2 + 0.0687\,T_{2\text{m}}h_{\text{ice}} - 0.0313\,h_{\text{ice}}^2 + 0.0087\,h_{\text{snow}}^3 \\
& + 0.0055\,h_{\text{snow}}^2T_{0\text{m}} - 0.0062\,h_{\text{snow}}^2T_{2\text{m}} + 0.0097\,h_{\text{snow}}^2h_{\text{ice}} - 0.0180\,h_{\text{snow}}T_{0\text{m}}^2 \\
& + 0.0287\,h_{\text{snow}}T_{0\text{m}}T_{2\text{m}} + 0.0210\,h_{\text{snow}}T_{0\text{m}}h_{\text{ice}} - 0.0469\,h_{\text{snow}}T_{2\text{m}}^2 - 0.0132\,h_{\text{snow}}T_{2\text{m}}h_{\text{ice}} \\
& - 0.0050\,h_{\text{snow}}h_{\text{ice}}^2 - 0.0193\,T_{0\text{m}}^3 + 0.0125\,T_{0\text{m}}^2T_{2\text{m}} - 0.0144\,T_{0\text{m}}^2h_{\text{ice}} - 0.0047\,T_{0\text{m}}T_{2\text{m}}^2 \\
& + 0.0218\,T_{0\text{m}}T_{2\text{m}}h_{\text{ice}} - 0.0093\,T_{0\text{m}}h_{\text{ice}}^2 + 0.0011\,T_{2\text{m}}^3 + 0.0070\,T_{2\text{m}}^2h_{\text{ice}} + 0.0028\,T_{0\text{m}}h_{\text{ice}}^2 \\
& + 0.0026\,h_{\text{ice}}^3
\end{aligned}
\tag{D1}
$$

https://doi.org/10.5194/egusphere-2025-3556
Preprint. Discussion started: 8 October 2025

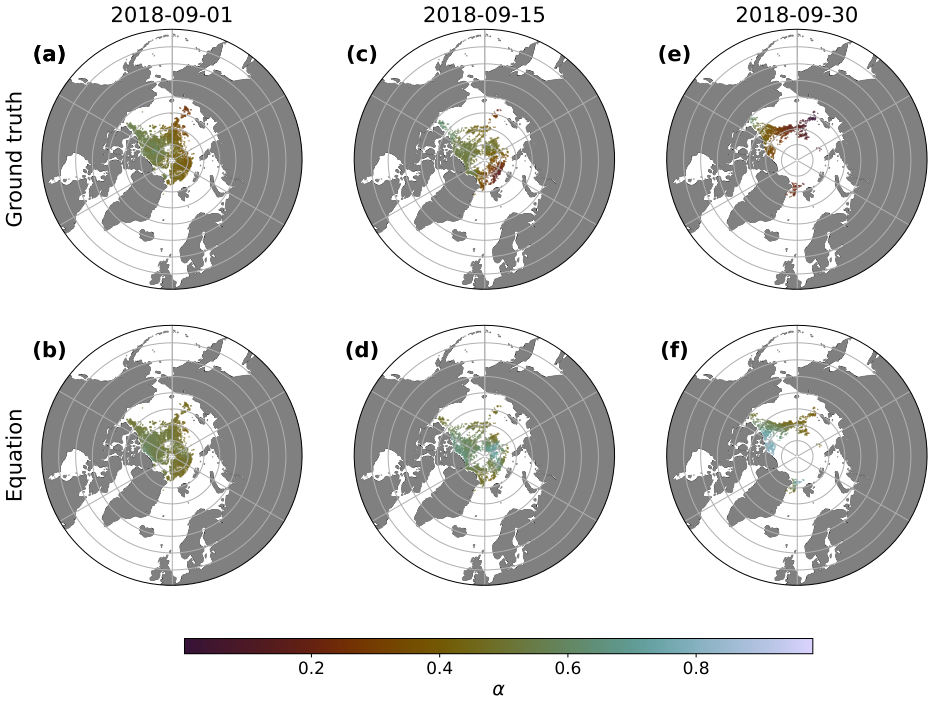

Figure E1. Comparison of sea ice albedo maps between the VIIRS product (ground truth) and Eq. 4 on September 1, 15 and 30, 2018.

Appendix E: Comparison of spatial maps between the VIIRS product and Equation 4

Figure E1 shows the differences in spatial maps between the VIIRS product (ground truth) and Eq. 4 exemplarily for September 1, 15 and 30, 2018.

Appendix F: Regional optimisation

Figure F1 displays the regionally optimised coefficients in their unitless form using the BFGS-optimiser which we plug in to Eq. 4 to compute the MSE on the validation set shown in Sec. 5, Fig. 10.

Appendix G: Monthly optimisation

Figure G1 displays the regionally optimised coefficients using the BFGS-optimiser which we plug in to Eq. 4 to compute the MSE on the validation set shown in Sec. 5, Fig. 10.

https://doi.org/10.5194/egusphere-2025-3556
Preprint. Discussion started: 8 October 2025

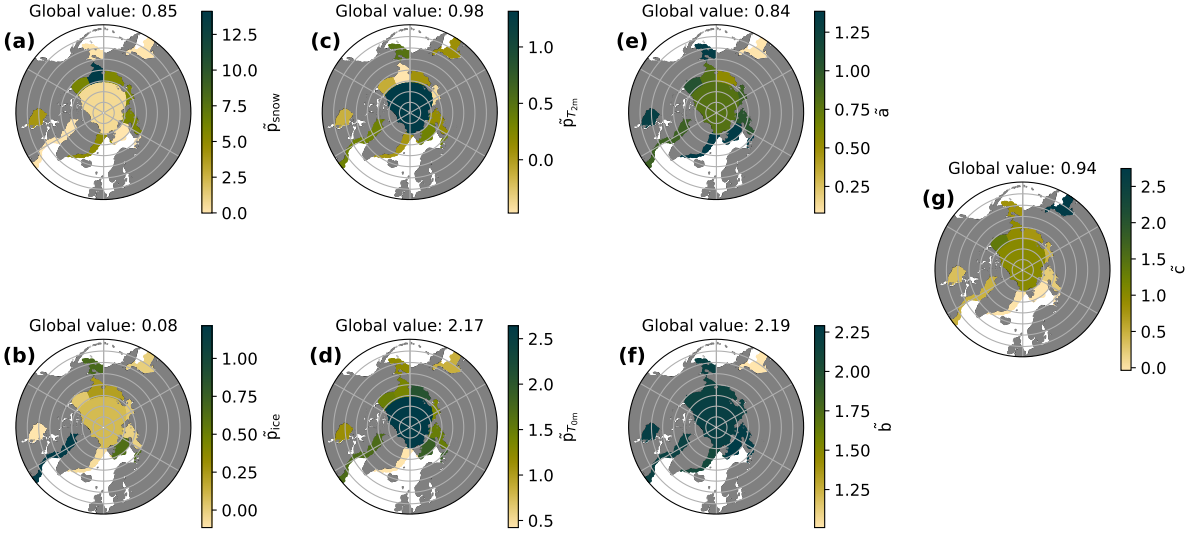

Figure F1. Regionally optimised coefficients of Eq. 4. The coefficients are unitless, meaning that they are rescaled by dividing by their standard deviations of the training set (2013–2018).

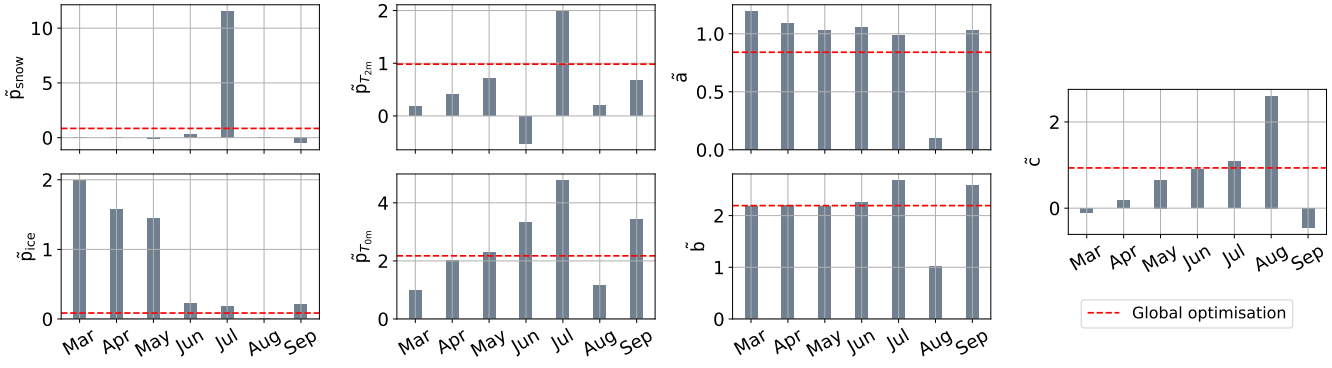

Figure G1. Monthly optimised coefficients of Eq. 4. The coefficients are unitless, meaning that they are rescaled by dividing by their standard deviations of the training set (2013–2018).

Author contributions. DWA developed the source code, performed the data processing and analyses and prepared all figures and tables. KW, AG, MMH, DS and VE contributed to the concept of the study and interpretation of the results and supported the analysis. DWA led the writing of the paper with contributions from KW and AG and feedback from all co-authors.

Competing interests. The authors declare that they have no conflict of interest.

https://doi.org/10.5194/egusphere-2025-3556
Preprint. Discussion started: 8 October 2025

Acknowledgements. DWA, KW and VE were funded by the Deutsche Forschungsgemeinschaft (DFG, German Research Foundation) through the Gottfried Wilhelm Leibniz Prize awarded to Veronika Eyring (Reference number EY 22/2-1). DWA and KW acknowledge support from the EERIE project (Grant Agreement No 101081383) funded by the European Union. Views and opinions expressed are however those of the authors only and do not necessarily reflect those of the European Union or the European Climate Infrastructure and Environment Executive Agency (CINEA). Neither the European Union nor the granting authority can be held responsible for them. This work has received funding from the Swiss State Secretariat for Education, Research and Innovation (SERI) under contract 22.00366. This work was funded by UK Research and Innovation (UKRI) under the UK government's Horizon Europe funding guarantee (Grants 10057890, 10049639, 10040510, 10040984). DWA was also supported by a fellowship of the German Academic Exchange Service (DAAD). KW acknowledges funding by the Collaborative Research Centre TRR 181 "Energy Transfers in Atmosphere and Ocean". VE and AG received funding for this study by the European Research Council (ERC) Synergy Grant "Understanding and modeling the Earth System with Machine Learning" (USMILE) under the EU Horizon 2020 research. AG also received funding from the Horizon Europe project "Artificial Intelligence for enhanced representation of processes and extremes in Earth System Models (AI4PEX)" (Grant agreement ID: 101137682). Support was provided to MMH by Schmidt Sciences, LLC. DS was supported by the Helmholtz Climate Initiative REKLIM (Regional Climate Change). This work used resources of the Deutsches Klimarechenzentrum (DKRZ) granted by its Scientific Steering Committee (WLA) under projects no. BD1083 and BD1377. We acknowledge the use of Fabio Crameri's Colour Maps (Crameri et al., 2020; Crameri, 2023) to ensure perceptual uniformity and accessibility of visual data representations throughout this work. DWA acknowledges the use of Blablador, developed under the Helmholtz AI initiative, to identify improvements in the writing style of an earlier version of the manuscript.

https://doi.org/10.5194/egusphere-2025-3556
Preprint. Discussion started: 8 October 2025

References

Beucler, T., Grundner, A., Shamekh, S., Ukkonen, P., Chantry, M., and Lagerquist, R.: Distilling Machine Learning's Added Value: Pareto Fronts in Atmospheric Applications, https://doi.org/10.48550/ARXIV.2408.02161, version Number: 1, 2024.

Bleck, R.: An oceanic general circulation model framed in hybrid isopycnic-Cartesian coordinates, Ocean Modelling, 4, 55–88, https://doi.org/10.1016/S1463-5003(01)00012-9, 2002.

Bracco, A., Brajard, J., Dijkstra, H. A., Hassanzadeh, P., Lessig, C., and Monteleoni, C.: Machine learning for the physics of climate, Nature Reviews Physics, 7, 6–20, https://doi.org/10.1038/s42254-024-00776-3, 2024.

Briegleb, B. and Light, B.: A Delta-Eddington Mutiple Scattering Parameterization for Solar Radiation in the Sea Ice Component of the Community Climate System Model, Tech. rep., UCAR/NCAR, https://doi.org/10.5065/D6B27S71, artwork Size: 5209 KB Medium: application/pdf, 2007.

Camps-Valls, G., Gerhardus, A., Ninad, U., Varando, G., Martius, G., Balaguer-Ballester, E., Vinuesa, R., Diaz, E., Zanna, L., and Runge, J.: Discovering causal relations and equations from data, Physics Reports, 1044, 1–68, https://doi.org/10.1016/j.physrep.2023.10.005, 2023.

Copernicus Climate Change Service: ERA5 hourly data on single levels from 1940 to present, https://doi.org/10.24381/CDS.ADBB2D47, 2018a.

Copernicus Climate Change Service: ERA5 hourly data on pressure levels from 1940 to present, https://doi.org/10.24381/CDS.BD0915C6, 2018b.

Crameri, F.: Scientific colour maps, https://doi.org/10.5281/ZENODO.1243862, language: en, 2023.

Crameri, F., Shephard, G. E., and Heron, P. J.: The misuse of colour in science communication, Nature Communications, 11, 5444, https://doi.org/10.1038/s41467-020-19160-7, 2020.

Cranmer, M., Sanchez-Gonzalez, A., Battaglia, P., Xu, R., Cranmer, K., Spergel, D., and Ho, S.: Discovering Symbolic Models from Deep Learning with Inductive Biases, https://doi.org/10.48550/ARXIV.2006.11287, publisher: arXiv Version Number: 2, 2020.

Curry, J. A., Schramm, J. L., and Ebert, E. E.: Sea Ice-Albedo Climate Feedback Mechanism, Journal of Climate, 8, 240–247, https://doi.org/10.1175/1520-0442(1995)008<0240:siacfm>2.0.co;2, publisher: American Meteorological Society, 1995.

Curry, J. A., Schramm, J. L., Perovich, D. K., and Pinto, J. O.: Applications of SHEBA/FIRE data to evaluation of snow/ice albedo parameterizations, Journal of Geophysical Research: Atmospheres, 106, 15 345–15 355, https://doi.org/10.1029/2000JD900311, 2001.

Danilov, S., Wang, Q., Timmermann, R., Iakovlev, N., Sidorenko, D., Kimmritz, M., Jung, T., and Schröter, J.: Finite-Element Sea Ice Model (FESIM), version 2, Geoscientific Model Development, 8, 1747–1761, https://doi.org/10.5194/gmd-8-1747-2015, 2015.

Danilov, S., Sidorenko, D., Wang, Q., and Jung, T.: The Finite-volumE Sea ice–Ocean Model (FESOM2), Geoscientific Model Development, 10, 765–789, https://doi.org/10.5194/gmd-10-765-2017, 2017.

De Franca, F. O., Virgolin, M., Kommenda, M., Majumder, M. S., Cranmer, M., Espada, G., Ingelse, L., Fonseca, A., Landajuela, M., Petersen, B., Glatt, R., Mundhenk, N., Lee, C. S., Hochhalter, J. D., Randall, D. L., Kamienny, P., Zhang, H., Dick, G., Simon, A., Burlacu, B., Kasak, J., Machado, M., Wilstrup, C., and Cavaz, W. G. L.: SRBench++: Principled Benchmarking of Symbolic Regression With Domain-Expert Interpretation, IEEE Transactions on Evolutionary Computation, pp. 1–1, https://doi.org/10.1109/TEVC.2024.3423681, 2024.

European Union-Copernicus Marine Service: Global Ocean Sea Ice Concentration Time Series REPROCESSED (EUMETSAT OSI-SAF), https://doi.org/10.48670/MOI-00136, 2015.

European Union-Copernicus Marine Service: Arctic Ocean Physics Reanalysis, https://doi.org/10.48670/MOI-00007, 2020.

https://doi.org/10.5194/egusphere-2025-3556
Preprint. Discussion started: 8 October 2025

Eyring, V., Bony, S., Meehl, G. A., Senior, C. A., Stevens, B., Stouffer, R. J., and Taylor, K. E.: Overview of the Coupled Model Intercomparison Project Phase 6 (CMIP6) experimental design and organization, Geoscientific Model Development, 9, 1937–1958, https://doi.org/10.5194/gmd-9-1937-2016, 2016.

Eyring, V., Collins, W. D., Gentine, P., Barnes, E. A., Barreiro, M., Beucler, T., Bocquet, M., Bretherton, C. S., Christensen, H. M., Dagon, K., Gagne, D. J., Hall, D., Hammerling, D., Hoyer, S., Iglesias-Suarez, F., Lopez-Gomez, I., McGraw, M. C., Meehl, G. A., Molina, M. J., Monteleoni, C., Mueller, J., Pritchard, M. S., Rolnick, D., Runge, J., Stier, P., Watt-Meyer, O., Weigel, K., Yu, R., and Zanna, L.: Pushing the frontiers in climate modelling and analysis with machine learning, Nature Climate Change, 14, 916–928, https://doi.org/10.1038/s41558-024-02095-y, 2024.

Flocco, D., Feltham, D. L., and Turner, A. K.: Incorporation of a physically based melt pond scheme into the sea ice component of a climate model, Journal of Geophysical Research: Oceans, 115, 2009JC005 568, https://doi.org/10.1029/2009JC005568, 2010.

Grenfell, T. C. and Maykut, G. A.: The Optical Properties of Ice and Snow in the Arctic Basin, Journal of Glaciology, 18, 445–463, https://doi.org/10.3189/S0022143000021122, 1977.

Grenfell, T. C. and Perovich, D. K.: Seasonal and spatial evolution of albedo in a snow-ice-land-ocean environment, Journal of Geophysical Research: Oceans, 109, 2003JC001 866, https://doi.org/10.1029/2003JC001866, 2004.

Grundner, A., Beucler, T., Gentine, P., and Eyring, V.: Data-Driven Equation Discovery of a Cloud Cover Parameterization, Journal of Advances in Modeling Earth Systems, 16, e2023MS003 763, https://doi.org/10.1029/2023MS003763, 2024.

Holland, M. M., Bailey, D. A., Briegleb, B. P., Light, B., and Hunke, E.: Improved Sea Ice Shortwave Radiation Physics in CCSM4: The Impact of Melt Ponds and Aerosols on Arctic Sea Ice, Journal of Climate, 25, 1413–1430, https://doi.org/10.1175/JCLI-D-11-00078.1, 2012.

Hunke, E. C. and Dukowicz, J. K.: An Elastic–Viscous–Plastic Model for Sea Ice Dynamics, Journal of Physical Oceanography, 27, 1849–1867, https://doi.org/10.1175/1520-0485(1997)027<1849:AEVPMF>2.0.CO;2, 1997.

Hunke, E. C., Lipscomb, W. H., and Turner, A. K.: Sea-ice models for climate study: retrospective and new directions, Journal of Glaciology, 56, 1162–1172, https://doi.org/10.3189/002214311796406095, 2010.

Hunke, E. C., Hebert, D. A., and Lecomte, O.: Level-ice melt ponds in the Los Alamos sea ice model, CICE, Ocean Modelling, 71, 26–42, https://doi.org/10.1016/j.ocemod.2012.11.008, 2013.

Hunke, E. C., Allard, R., Bailey, D. A., Blain, P., Craig, A., Dupont, F., DuVivier, A. K., Grumbine, R., Hebert, D. A., Holland, M. M., Jeffery, N., Lemieux, J., Osinski, R., Rasmussen, T., Ribergaard, M., Roach, L., Roberts, A., Turner, M., and Winton, M.: CICE-Consortium/Icepack: Icepack 1.4.0, https://doi.org/10.5281/ZENODO.10056496, language: en, 2023.

Huntingford, C., Nicoll, A. J., Klein, C., and Ahmad, J. A.: Potential for equation discovery with AI in the climate sciences, Earth System Dynamics, 16, 475–495, https://doi.org/10.5194/esd-16-475-2025, 2025.

Jäkel, E., Becker, S., Sperzel, T. R., Niehaus, H., Spreen, G., Tao, R., Nicolaus, M., Dorn, W., Rinke, A., Brauchle, J., and Wendisch, M.: Observations and modeling of areal surface albedo and surface types in the Arctic, The Cryosphere, 18, 1185–1205, https://doi.org/10.5194/tc-18-1185-2024, 2024.

Key, J., Wang, X., Lui, Y., and NOAA CDR Program: NOAA Climate Data Record (CDR) of AVHRR Polar Pathfinder Extended (APP-X) Cryosphere, Version 1 (Version Superseded), https://doi.org/10.7289/V5MK69W6, 2016.

Key, J. R., Wang, X., Stoeve, J. C., and Fowler, C.: Estimating the cloudy-sky albedo of sea ice and snow from space, Journal of Geophysical Research: Atmospheres, 106, 12 489–12 497, https://doi.org/10.1029/2001JD900069, 2001.

https://doi.org/10.5194/egusphere-2025-3556
Preprint. Discussion started: 8 October 2025

Kwok, R.: Arctic sea ice thickness, volume, and multiyear ice coverage: losses and coupled variability (1958–2018), Environmental Research Letters, 13, 105 005, https://doi.org/10.1088/1748-9326/aae3ec, 2018.

Light, B., Smith, M. M., Perovich, D. K., Webster, M. A., Holland, M. M., Linhardt, F., Raphael, I. A., Clemens-Sewall, D., Macfarlane, A. R., Anhaus, P., and Bailey, D. A.: Arctic sea ice albedo: Spectral composition, spatial heterogeneity, and temporal evolution observed during the MOSAiC drift, Elementa: Science of the Anthropocene, 10, 000 103, https://doi.org/10.1525/elementa.2021.000103, 2022.

Liu, W., Yang, S., Chen, D., Zha, J., Zhang, G., Zhang, Z., Zhang, T., Xu, L., Hu, X., and Deng, K.: Rapid Acceleration of Arctic Near-Surface Wind Speed in a Warming Climate, Geophysical Research Letters, 51, e2024GL109 385, https://doi.org/10.1029/2024GL109385, 2024.

Meier, W. and Stewart, J.: Arctic and Antarctic Regional Masks for Sea Ice and Related Data Products, Version 1, https://doi.org/10.5067/CYW3O8ZUNIWC, 2023.

Nelder, J. A. and Mead, R.: A Simplex Method for Function Minimization, The Computer Journal, 7, 308–313, https://doi.org/10.1093/comjnl/7.4.308, 1965.

Niehaus, H., Spreen, G., Istomina, L., and Nicolaus, M.: Regional and seasonal evolution of melt ponds on Arctic sea ice, https://doi.org/10.5194/egusphere-2024-3127, 2024.

Nocedal, J. and Wright, S. J.: Numerical optimization, Springer series in operations research and financial engineering, Springer, New York, NY, second edition edn., ISBN 978-0-387-30303-1 978-0-387-40065-5, 2006.

Notz, D. and Community, S.: Arctic Sea Ice in CMIP6, Geophysical Research Letters, 47, e2019GL086 749, https://doi.org/10.1029/2019GL086749, 2020.

Parkinson, C. L. and Washington, W. M.: A large-scale numerical model of sea ice, Journal of Geophysical Research: Oceans, 84, 311–337, https://doi.org/10.1029/JC084iC01p00311, 1979.

Paszke, A., Gross, S., Massa, F., Lerer, A., Bradbury, J., Chanan, G., Killeen, T., Lin, Z., Gimelshein, N., Antiga, L., Desmaison, A., Kopf, A., Yang, E., DeVito, Z., Raison, M., Tejani, A., Chilamkurthy, S., Steiner, B., Fang, L., Bai, J., and Chintala, S.: PyTorch: An Imperative Style, High-Performance Deep Learning Library, in: Advances in Neural Information Processing Systems 32, pp. 8024–8035, Curran Associates, Inc., http://papers.neurips.cc/paper/9015-pytorch-an-imperative-style-high-performance-deep-learning-library.pdf, 2019.

Pedregosa, F., Varoquaux, G., Gramfort, A., Michel, V., Thirion, B., Grisel, O., Blondel, M., Prettenhofer, P., Weiss, R., Dubourg, V., and others: Scikit-learn: Machine learning in Python, Journal of machine learning research, 12, 2825–2830, 2011.

Peng, J., Yu, Y., Yu, P., and Liang, S.: The VIIRS Sea-Ice Albedo Product Generation and Preliminary Validation, Remote Sensing, 10, 1826, https://doi.org/10.3390/rs10111826, publisher: MDPI AG, 2018.

Perovich, D. K.: Monograph 96-1 The Optical Properties of Sea Ice, https://api.semanticscholar.org/CorpusID:21416227, 1996.

Perovich, D. K., Grenfell, T. C., Light, B., and Hobbs, P. V.: Seasonal evolution of the albedo of multiyear Arctic sea ice, Journal of Geophysical Research: Oceans, 107, https://doi.org/10.1029/2000JC000438, 2002.

Pirazzini, R.: Challenges in Snow and Ice Albedo Parameterizations, Geophysica, 45, 41–62, 2009.

Pistone, K., Eisenman, I., and Ramanathan, V.: Observational determination of albedo decrease caused by vanishing Arctic sea ice, Proceedings of the National Academy of Sciences, 111, 3322–3326, https://doi.org/10.1073/pnas.1318201111, 2014.

Pithan, F. and Mauritsen, T.: Arctic amplification dominated by temperature feedbacks in contemporary climate models, Nature Geoscience, 7, 181–184, https://doi.org/10.1038/ngeo2071, publisher: Springer Science and Business Media LLC, 2014.

Rasp, S., Pritchard, M. S., and Gentine, P.: Deep learning to represent subgrid processes in climate models, Proceedings of the National Academy of Sciences, 115, 9684–9689, https://doi.org/10.1073/pnas.1810286115, 2018.

https://doi.org/10.5194/egusphere-2025-3556
Preprint. Discussion started: 8 October 2025

Ricker, R., Hendricks, S., Kaleschke, L., Tian-Kunze, X., King, J., and Haas, C.: A weekly Arctic sea-ice thickness data record from merged CryoSat-2 and SMOS satellite data, The Cryosphere, 11, 1607–1623, https://doi.org/10.5194/tc-11-1607-2017, 2017.

Rostosky, P., Spreen, G., Farrell, S. L., Frost, T., Heygster, G., and Melsheimer, C.: Snow Depth Retrieval on Arctic Sea Ice From Passive Microwave Radiometers—Improvements and Extensions to Multiyear Ice Using Lower Frequencies, Journal of Geophysical Research: Oceans, 123, 7120–7138, https://doi.org/10.1029/2018JC014028, 2018.

Screen, J. A. and Simmonds, I.: Increasing fall-winter energy loss from the Arctic Ocean and its role in Arctic temperature amplification, Geophysical Research Letters, 37, 2010GL044 136, https://doi.org/10.1029/2010GL044136, 2010.

Selivanova, J., Iovino, D., and Cocetta, F.: Past and future of the Arctic sea ice in High-Resolution Model Intercomparison Project (HighResMIP) climate models, The Cryosphere, 18, 2739–2763, https://doi.org/10.5194/tc-18-2739-2024, 2024.

Smedsrud, L. H., Esau, I., Ingvaldsen, R. B., Eldevik, T., Haugan, P. M., Li, C., Lien, V. S., Olsen, A., Omar, A. M., Otterå, O. H., Risebrobakken, B., Sandø, A. B., Semenov, V. A., and Sorokina, S. A.: The role of the Barents Sea in the Arctic climate system, Reviews of Geophysics, 51, 415–449, https://doi.org/10.1002/rog.20017, 2013.

Song, W., Jiang, S., Camps-Valls, G., Williams, M., Zhang, L., Reichstein, M., Vereecken, H., He, L., Hu, X., and Shi, L.: Towards data-driven discovery of governing equations in geosciences, Communications Earth & Environment, 5, 589, https://doi.org/10.1038/s43247-024-01760-6, 2024.

Spreen, G., Kaleschke, L., and Heygster, G.: Sea ice remote sensing using AMSR-E 89-GHz channels, Journal of Geophysical Research: Oceans, 113, 2005JC003 384, https://doi.org/10.1029/2005JC003384, 2008.

Streffing, J., Sidorenko, D., Semmler, T., Zampieri, L., Scholz, P., Andrés-Martínez, M., Koldunov, N., Rackow, T., Kjellsson, J., Goessling, H., Athanase, M., Wang, Q., Hegewald, J., Sein, D. V., Mu, L., Fladrich, U., Barbi, D., Gierz, P., Danilov, S., Juricke, S., Lohmann, G., and Jung, T.: AWI-CM3 coupled climate model: description and evaluation experiments for a prototype post-CMIP6 model, Geoscientific Model Development, 15, 6399–6427, https://doi.org/10.5194/gmd-15-6399-2022, 2022.

Stroeve, J. and Notz, D.: Changing state of Arctic sea ice across all seasons, Environmental Research Letters, 13, 103 001, https://doi.org/10.1088/1748-9326/aade56, 2018.

Tschudi, M., Meier, W. N., Stewart, J. S., Fowler, C., and Maslanik, J.: Polar Pathfinder Daily 25 km EASE-Grid Sea Ice Motion Vectors, https://doi.org/10.5067/INAWUWO7QH7B, 2019a.

Tschudi, M., Meier, W. N., Stewart, J. S., Fowler, C., and Maslanik, J.: EASE-Grid Sea Ice Age, https://doi.org/10.5067/UTAV7490FEPB, 2019b.

Vance, T. C., Huang, T., and Butler, K. A.: Big data in Earth science: Emerging practice and promise, Science, 383, eadh9607, https://doi.org/10.1126/science.adh9607, 2024.

Virtanen, P., Gommers, R., Oliphant, T. E., Haberland, M., Reddy, T., Cournapeau, D., Burovski, E., Peterson, P., Weckesser, W., Bright, J., Van Der Walt, S. J., Brett, M., Wilson, J., Millman, K. J., Mayorov, N., Nelson, A. R. J., Jones, E., Kern, R., Larson, E., Carey, C. J., Polat, , Feng, Y., Moore, E. W., VanderPlas, J., Laxalde, D., Perktold, J., Cimrman, R., Henriksen, I., Quintero, E. A., Harris, C. R., Archibald, A. M., Ribeiro, A. H., Pedregosa, F., Van Mulbregt, P., SciPy 1.0 Contributors, Vijaykumar, A., Bardelli, A. P., Rothberg, A., Hilboll, A., Kloeckner, A., Scopatz, A., Lee, A., Rokem, A., Woods, C. N., Fulton, C., Masson, C., Häggström, C., Fitzgerald, C., Nicholson, D. A., Hagen, D. R., Pasechnik, D. V., Olivetti, E., Martin, E., Wieser, E., Silva, F., Lenders, F., Wilhelm, F., Young, G., Price, G. A., Ingold, G.-L., Allen, G. E., Lee, G. R., Audren, H., Probst, I., Dietrich, J. P., Silterra, J., Webber, J. T., Slavič, J., Nothman, J., Buchner, J., Kulick, J., Schönberger, J. L., De Miranda Cardoso, J. V., Reimer, J., Harrington, J., Rodríguez, J. L. C., Nunez-Iglesias, J., Kuczynski, J., Tritz, K., Thoma, M., Newville, M., Kümmerer, M., Bolingbroke, M., Tartre, M., Pak, M., Smith, N. J., Nowaczyk, N., Shebanov, N.,

https://doi.org/10.5194/egusphere-2025-3556
Preprint. Discussion started: 8 October 2025

Pavlyk, O., Brodtkorb, P. A., Lee, P., McGibbon, R. T., Feldbauer, R., Lewis, S., Tygier, S., Sievert, S., Vigna, S., Peterson, S., More, S., Pudlik, T., Oshima, T., Pingel, T. J., Robitaille, T. P., Spura, T., Jones, T. R., Cera, T., Leslie, T., Zito, T., Krauss, T., Upadhyay, U., Halchenko, Y. O., and Vázquez-Baeza, Y.: SciPy 1.0: fundamental algorithms for scientific computing in Python, Nature Methods, 17, 261–272, https://doi.org/10.1038/s41592-019-0686-2, 2020.

Webster, M. A., Holland, M., Wright, N. C., Hendricks, S., Hutter, N., Itkin, P., Light, B., Linhardt, F., Perovich, D. K., Raphael, I. A., Smith, M. M., Von Albedyll, L., and Zhang, J.: Spatiotemporal evolution of melt ponds on Arctic sea ice, Elementa: Science of the Anthropocene, 10, 000 072, https://doi.org/10.1525/elementa.2021.000072, 2022.

Yamagami, Y., Watanabe, M., Mori, M., and Ono, J.: Barents-Kara sea-ice decline attributed to surface warming in the Gulf Stream, Nature Communications, 13, 3767, https://doi.org/10.1038/s41467-022-31117-6, 2022.

Zampieri, L., Kauker, F., Fröhle, J., Sumata, H., Hunke, E. C., and Goessling, H. F.: Impact of Sea-Ice Model Complexity on the Performance of an Unstructured-Mesh Sea-Ice/Ocean Model under Different Atmospheric Forcings, Journal of Advances in Modeling Earth Systems, 13, e2020MS002 438, https://doi.org/10.1029/2020MS002438, 2021.

Zampieri, L., Arduini, G., Holland, M., Keeley, S. P. E., Mogensen, K., Shupe, M. D., and Tietsche, S.: A Machine Learning Correction Model of the Winter Clear-Sky Temperature Bias over the Arctic Sea Ice in Atmospheric Reanalyses, Monthly Weather Review, 151, 1443–1458, https://doi.org/10.1175/MWR-D-22-0130.1, 2023.

Zanna, L. and Bolton, T.: Data-Driven Equation Discovery of Ocean Mesoscale Closures, Geophysical Research Letters, 47, e2020GL088 376, https://doi.org/10.1029/2020GL088376, 2020.

Zhuang, J., raphael dussin, Huard, D., Bourgault, P., Banihirwe, A., Raynaud, S., Malevich, B., Schupfner, M., Filipe, Gauthier, C., Levang, S., Jüling, A., Almansi, M., RichardScottOZ, RondeauG, Rasp, S., Smith, T. J., Mares, B., Stachelek, J., Plough, M., Pierre, Bell, R., Caneill, R., and Li, X.: pangeo-data/xESMF: v0.8.8, https://doi.org/10.5281/ZENODO.4294774, 2024.

Årthun, M., Eldevik, T., Smedsrud, L. H., Skagseth, , and Ingvaldsen, R. B.: Quantifying the Influence of Atlantic Heat on Barents Sea Ice Variability and Retreat*, Journal of Climate, 25, 4736–4743, https://doi.org/10.1175/JCLI-D-11-00466.1, 2012.